EFFICIENT ALGORITHMS FOR PARALLEL EXCITATION AND PARALLEL IMAGING WITH LARGE ARRAYS

A Dissertation

by

SHUO FENG

Submitted to the Office of Graduate and Professional Studies of
Texas A&M University
in partial fulfillment of the requirements for the degree of

DOCTOR OF PHILOSOPHY

Chair of Committee,	Jim Ji
Committee Members,	Costas Georghiades
	Mary McDougall
	Steven Wright
Head of Department,	Chanan Singh

August 2013

Major Subject: Electrical Engineering

ABSTRACT

During the past two decades, techniques and devices were developed to transmit and receive signals with a phased array instead of a single coil in the MRI (Magnetic Resonance Imaging) system. The two techniques to simultaneously transmit and receive RF signals using phased arrays are called parallel excitation (pTx) and parallel imaging (PI), respectively. These two techniques lead to shorter transmit pulses for higher imaging quality and faster data acquisition correspondingly.

This dissertation focuses on improving the efficiency of the pTx pulse design and the PI reconstruction in MRI. Both PI and pTx benefit from the increased number of elements of the array. However, efficiency concerns may arise which include: (1) In PI, the computation cost of the reconstructions and the achievable acceleration factors and (2) in pTx, the pulse design speed and memory cost. The work presented in this dissertation addresses these issues.

First, a correlation based channel reduction algorithm is developed to reduce the computation cost of PI reconstruction. In conventional k-domain methods, the individual channel data is reconstructed via linear interpolation of the neighbourhood data from all channels. In this proposed algorithm, we choose only a subset of the channels based on the spatial correlation. The results have shown that the computation cost can be significantly reduced with similar or higher reconstruction accuracy.

Then, a new parallel imaging method named parallel imaging using localized receive arrays with Sinc interpolation(PILARS) is proposed to improve the actual acceleration factor and to reduce the computation cost. It employs the local support of individual coils and pre-determines the magnitude of the reconstruction coeffi-

cients. Thus, it requires much less auto-calibration signals (ACS) data and achieves higher acceleration factors. The results show that this method can increase the acceleration factor and the reconstruction speed while achieving the same level of reconstruction quality.

Finally, a fast pTx pulse design method is proposed to accelerate the design speed. This method is based on the spatial domain pulse design method and can be used to accelerate similar methods. We substitute the two computational expensive matrix-vector multiplications in the conjugate gradient (CG) solver with gridding and fast Fourier transform (FFT). Theoretical and simulation results have shown that the design speed can be improved by 10 times. Meanwhile, the memory cost is reduced by 10^3 times. This breaks the memory burden of implementing pulse designs on GPU which enables further accelerations.

ACKNOWLEDGEMENTS

I would like to thank everyone who has guided and helped me to make this work possible. There are so many people to thanked to and there are so many things I feel deeply grateful for. This is a great journey.

I would like to start to thank my committee chair, Dr. Jim Ji. As the chair of my committee and my principal advisor, Dr. Ji provides plentiful of educations, supports and constant encouragement throughout the full course of my Ph.D research. Also I'd like to thank Dr. Wright for his support and arrangement to all my experiments done in Magnetic Resonance System Lab. I would also like to thank my committee Dr. Mary McDougall and Dr. Costas Georghiades for their insight and helpful comments and discussions on my work.

I would like to thank all my colleagues in my lab who offered various supports during the course of my research. Specifically, I would like to thank Ying Dong and Ching-Hua Chang for all the helps and ideas provided, John Bosshard and Neal Hollingsworth for the time and help with my experiments and for providing insights into experiment phenomena. I'd like to thank all my group mates Yinan Liu, Yuttapong Jiraraksopakun, Xiaoxi Ou, Harneet Singh, Gregory Whitehead and Nibal Arzouni for the wonderful and memorable days we've spent together. Also to everyone who has made my great experience at Texas A&M University. Many thanks to all my sources of funding including National Science Foundation under award number 0748180. And last but least, thanks to my parents, my fiancé Fangfang Wang and friends for the unwavering supports through these busy and stressful years of graduate school.

NOMENCLATURE

2D	Two Dimensional
3D	Three Dimensional
ACS	Auto Calibration Signals
CG	Conjugate Gradient
FE	Frequency Encoding
FFT	Fast Fourier Transform
FID	Free Induction Decay
FOV	Field of View
FOX	Field of Excitation
GPGPU	General-purpose Graphics Processing Unit
GPU	Graphics Processing Unit
GRE	Gradient Echo
GRAPPA	Generalized Autocalibrating Partially Parallel Acquisitions
MCMLI	Multicolumn Multiline Interpolation
MRI	Magnetic Resonance Imaging
NMR	Nuclear Magnetic Resonance
NRMSE	Normalized Root Mean Square Error
PE	Phase Encoding
PI	Parallel Imaging
PILARS	Parallel Magnetic Resonance Imaging using Localized Receive Arrays with Sinc Interpolation

PILS	Partially Parallel Imaging with Localized Sensitivities
pTx	Prallel Excitation
RF	Radio Frequency
ROI	Region of Interest
SAR	Specific Absorption Rate
SE	Spin Echo
SEA	Single Echo Acquisition
SENSE	Sensitivity Encoding
SMASH	Simultaneous Acquisition of Spatial Harmonics
SNR	Signal to Noise Ratio
STA	Small Tip-angle Approximation

TABLE OF CONTENTS

LIST OF FIGURES

FIGURE Page

LIST OF TABLES

TABLE Page

1. INTRODUCTION

1.1 Array for Excitation and Reception

RF coils play a key role in MRI as to transmit the excitation RF signal and receive the free induction decay (FID) RF signal. Conventionally, single birdcage coil is used for both the signal transmission and reception. Hitherto, phased arrays, especially the large arrays with large number of element coils, have been used to replace or supplement the single birdcage coil in MRI.

The application of phased array in MRI for signal reception initially arose to increase the the signal-to-noise ratio (SNR) [39]. The sum of squares algorithm for combinating individual channel images is proposed to be optimal in term of SNR. Sonn after, the spatial encoding provided by the spatial receive sensitivity of multiple coils had been explored and used to accelerate the data acquisition process. This technique is called parallel imaging (pMRI). Less data is acquired and the image is reconstructed using the spatial sensitivity information. Scan time is reduced proportional to the amount of skipped data in acquisition but the SNR is lost at the same time. However, the other technique development from the increase of main field strength to the improved low noise hardware offered MRI with higher SNR. And it becomes acceptable to trade the SNR for faster imaging speed.

Due to the fact that the acceleration is benefited from the additional spatial information, the increased number of elements in array promise higher potential accelerations for parallel imaging. Two phase arrays with a large number of channels are given in Fig. 1.1 and Fig. 1.2. The single echo acquisition (SEA)[31] method even goes to the extremity of completely eliminating the phase encoding and the maximum acceleration is achieved.

Figure 1.1: The SEA linear array built in Texas A&M University with 64 channels

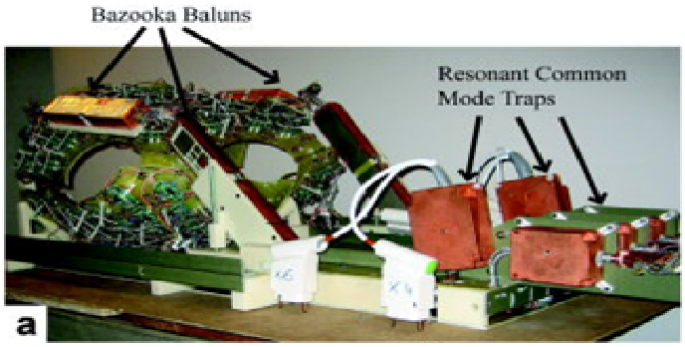

Figure 1.2: The 128 channel body array built in Massachusetts General Hospital

Phased arrays are also used for signal transmission in MRI to perform RF shimming [30, 45]. The goal is to compensate the main field inhomogeneity by controlling the transmit power of each shimming coil. Parallel excitation (pTx) has been proposed and proven to be the more effective in correcting field inhomogeneity issues more accurately and with lower specific absorption rate (SAR). More channels for

parallel transmission array also increase the degree of freedom of parallel excitation pulse design and provides improved performance. Transmit array examples are shown in Fig. 1.3 and Fig. 1.4.

Figure 1.3: 32 channel lattice transmission line array [1]

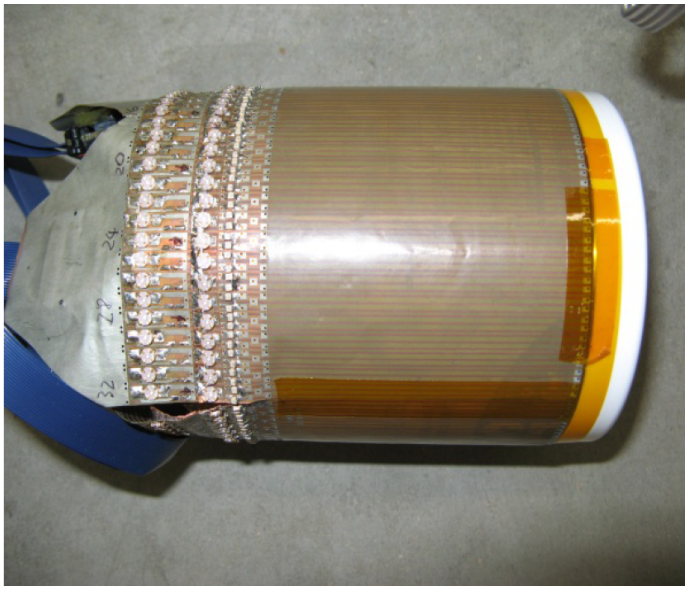

Figure 1.4: The 64 channel tranceive array built in MRSL, TAMU

Thus, it is the developing tendency that the number of channels in the phased

array will increase for both parallel imaging and parallel excitation.

1.2 Motivations

Although parallel excitation and parallel imaging are intrinsically benefited from more elements in the coil arrays, new challenges arise as well.

The first challenge is the increased computation cost for the reconstruction using parallel imaging methods. The amount of data to be processed increase linearly with the number of channels in the array and the actual computation cost can increase quadratically for certain parallel imaging methods.

The second challenge is the degraded acceleration provided by the k-domain parallel imaging methods. Interpolation coefficients in k-domain pMRI methods require additional calibration data which will reduced the actual achieved acceleration.

Finally, parallel excitation pulse design is time consuming comparing to the real time design goal.The design computation load increases linearly with the increased number of channels.

All these new challenges arose with large arrays are in the category of efficiency concerns. This dissertation is motivated by solving these efficiency concerns so that the benefit of using large arrays in MRI can be most enjoyed.

1.3 Dissertation Outline and Contributions

In Section 2, the background of MRI, parallel imaging and parallel excitation are introduced. Then, three major contribution work are introduced consecutively.

The contribution of this dissertation includes three major parts:

First, we propose a correlation based channel reduction algorithm to reduce the computation cost of PI reconstruction. In conventional k-domain methods, the individual channel data is reconstructed via linear interpolation of neighbourhood data from all channels. In this proposed algorithm, we choose only a subset of the channels

based on the spatial correlation. The computation cost can be significantly reduced with similar or higher reconstruction accuracy. This is described in Section 3.

Then, a new parallel imaging method named PILARS is proposed to improve the actual acceleration factor and reduce the computation cost. It employs the local support of individual coils and pre-determines the magnitude of the reconstruction coefficients. Thus, it requires much less auto-calibration signals (ACS) data to estimate the parameters and keeps the acceleration factor higher than the conventional k-domain methods. The proposed method can increase the actual acceleration factor and the reconstruction speed with the same level of reconstruction error comparing to the several conventional methods. This is described in Section 4.

Finally, a fast pulse design method is proposed to accelerate the design speed. This method is based on the spatial domain pulse design method and can be used to accelerate the designs of any methods related to it. We substitute the two computational expensive matrix-vector multiplications in the conjugate gradient (CG) solver with gridding and fast Fourier transform (FFT). Theoretical and simulation results have shown that the design speed can be improved by 10 times. Meanwhile, the memory cost is reduced by 10^3 times. This breaks the memory burden of implementing pulse designs on GPU and promises another $10\times$ design acceleration. This is described in Section 5.

2. BACKGROUND

2.1 Magnetic Resonance Imaging Basics

In this section, we provide an overview of Magnetic resonance imaging (MRI). Only the signal transmission and the signal detection part is explained with mathematical description while the other parts in MRI are briefly discussed.

MRI is a non-invasive imaging methodology comparing to computed tomography (CT) and X-ray imaging. It provides good contrast between the different soft tissues such as brain, heart and cancer. The fundamental physical phenomenon in MRI is given below. When a subject is placed in a strong magnetic field, a portion of the nuclear spins will become aligned with the main field of strength B_0 and precess along it at Larmor freqency $\omega_0 = \gamma B_0$, where γ is the gyromagnetic ratio. The spins are able to absorb electromagnetic signal at the same frequency to jump into higher energy state and then release electromagnetic signal out when jumping back to the original energy level as shown in Fig. 2.1. The Larmor frequency of hydrogen proton is in the range of radio frequency (RF). A MRI imaging period starts from transmit RF signal to excite the spins and ends when the released RF signal is detected. RF coils are used for the signal transmission and detection.

During the signal transmission process, Bloch equation describes the relation between the excited transverse magnetization, the excitation RF signal and the applied excitation gradient. Assume that the main field is in the z-direction and a reference frame rotating about z at Larmor frequency $\omega_0 = \gamma B_0$ is used. The following Bloch

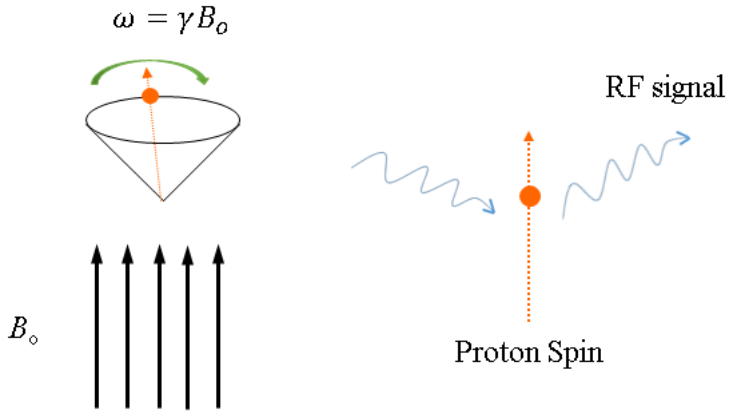

Figure 2.1: Larmor frequency and signal formation

equation is given without consideration of the relaxation effect,

$$\frac{d}{dt}\begin{pmatrix} M_x(\vec{r},t) \\ M_y(\vec{r},t) \\ M_z(\vec{r},t) \end{pmatrix} = \lambda \begin{pmatrix} 0 & \vec{G}(t)\cdot\vec{r} & -B_{1,y}(t) \\ -\vec{G}(t)\cdot\vec{r} & 0 & B_{1,x}(t) \\ B_{1,y}(t) & -B_{1,x}(t) & 0 \end{pmatrix} \begin{pmatrix} M_x(\vec{r},t) \\ M_y(\vec{r},t) \\ M_z(\vec{r},t) \end{pmatrix} \tag{2.1}$$

where $\vec{M}(\vec{r},t) = M_x(\vec{r},t)i + M_y(\vec{r},t)j + M_z(\vec{r},t)k$ is the magnetization at spatial location $\vec{r}$, $\vec{G}(t)$ is the applied time varying gradient, $\vec{G}(t)\cdot\vec{r}$ is the z-direction field generated by the gradient and $B_{1,x}$ and $B_{1,y}$ are the x-component and y-component of the applied RF pulse. Traditionally, a Sinc RF pulse will be used along with a constant z-direction gradient to excite a thin slice as shown in Fig. 2.2. This ability to do selective imaging is a key advantage of MRI comparing to other imaging modalities.

In order to do imaging, the spatial information of the object is encoded into the received RF signal. This is done by using gradient coils to generate gradient field. Gradient field is a spatially varying magnetic field which is in the same direction as the main field. With the gradient, spins at different spatial locations are processing

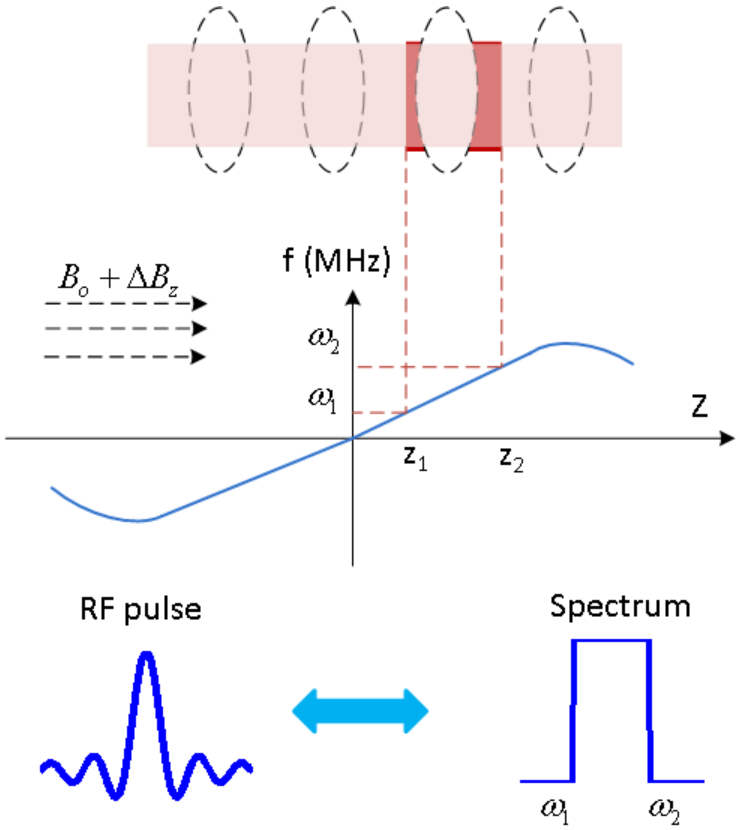

Figure 2.2: Constant slice selection gradient in the main field direction and the Sinc excitation RF pulse

at a unique Larmor frequency and the received RF signal are composed of frequency components representing the signal strength from a particular spatial location. The gradient applied during the data acquisition is named frequency encoding (FE) gradient and the gradent that generates similar encoding in the perpendicular direction is called phase encoding (PE) gradient. The relationship between the proton density and the received RF signal is described as,

$$S(t_f) = \int_{-\infty}^{\infty} \int_{-\infty}^{\infty} I(x,y) e^{+jk_y y + jk_x x} dx dy \tag{2.2}$$

where

$I(x, y)$ represents the proton density of the underlining object

$k_y = \gamma G_y T_p$

$k_x = \gamma G_x t_f$

$Tp =$ the phase encoding pulse length

$G_y =$ the amplitude of the phase encoding gradient

$G_x =$ the amplitude of the frequency encoding gradient

$T_p =$ the duration of the phase encoding gradient

$t_f =$ the time since the beginning of the frequency encoding gradient pulse

As can be seen, the received RF signal and the underlining desired image form a Fourier pair. The inverse Fourier transform to reconstruct the image from acquired data. We call the frequency space in which the data is acquired the k-space. For each phase encoding, we read out one line of the k-space. To perform a two dimensional (2D) imaging, different PE steps need to be applied till the whole 2D data is acquired. A illustrative image of the MRI scanner is shown in Fig. 2.3 with gradient coils and Rf coils.

2.2 Parallel Imaging

Parallel imaging methods can be categorized by the domain in which the reconstruction is formulated: the spatial domain method, the k-domain method and the hybrid method. In the following sections, two spatial domain methods SENSE and PILS will be introduced first. Then, several k-domain methods will be are explained in detail along with the validation method. In the end, the efficiency concerns in k-domain parallel imaging is discussed.

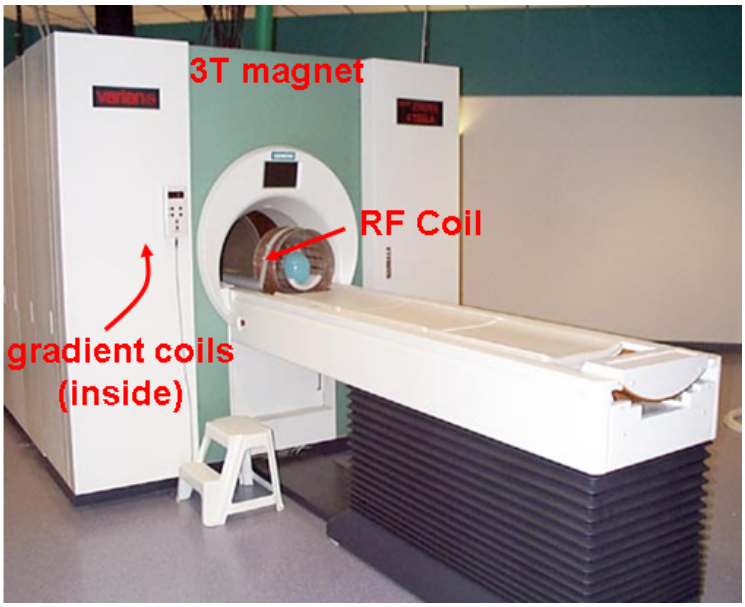

Figure 2.3: A typical MRI scanner with gradient coils and RF coils

2.2.1 SENSE: Sensitivity Encoding

The idea of SENSE [36] is that the imaging speed can be accelerated by sampling a sparser k-space compared to the Nyquist rate, e.g. less phase encoding (PE) steps. And on the Cartesian sampling grid, the lower sampling rate will lead to a predictable aliasing in the spatial domain (image folding). The additional information of array's reception sensitivity is encoded in the aliased individual channel image. With the receive sensitivity of each channel as prior-knowledge, a set of linear equations can be built that relate the underlining true image and each of the aliased channel image. Then, the true image can be reconstructed by solving the linear equations.

For simplicity concern, the SENSE method on Cartesian grid will be formulated here. Suppose the full size of the image to be reconstructed $I(x_i, y_j)$ are N_p and N_f in the PE and FE direction respectively. With an accelerated acquisition by a factor of R in the PE direction, the FOV is reduced to the size of $\frac{N_p}{R}$ by N_f. Assume there

are a total number of L reception channels and the coil sensitivity $S_l(x, y)$ is known for each channel for the l-th channel. Then, the SENSE equation for a single pixel at (x_i, y_j) in aliased image can be formulated as,

$$\begin{pmatrix} I_1(x_i, y_j) \\ I_2(x_i, y_j) \\ \vdots \\ I_L(x_i, y_j) \end{pmatrix}_{L\times 1} = \begin{pmatrix} S_1(x_i, y_j) & S_1(x_i, y_j + \frac{N_p}{R}) & \cdots & S_1(x_i, y_j + N_p) \\ S_2(x_i, y_j) & S_2(x_i, y_j + \frac{N_p}{R}) & \cdots & S_2(x_i, y_j + N_p) \\ \vdots & \vdots & \vdots & \vdots \\ S_L(x_i, y_j) & S_L(x_i, y_j + \frac{N_p}{R}) & \cdots & S_L(x_i, y_j + N_p) \end{pmatrix}_{L\times R} \cdot \begin{pmatrix} I(x_i, y_j + \frac{0}{R}N_p) \\ I(x_i, y_j + \frac{1}{R}N_p) \\ \vdots \\ I(x_i, y_j + \frac{R}{R}N_p) \end{pmatrix}_{R\times 1} \tag{2.3}$$

where $I_l(x_i, y_j)$ is the pixel value at (x_i, y_j) in the acquired aliasing image of the l-th channel and I is the image to be solved. x denotes the coordinates in the FE direction and denotes the coordinates in the PE direction with index $i = 1, 2, \cdots, N_f$ and $j = 1, 2, \cdots, \frac{N_p}{R}$ respectively. So generally, for each pixel in the aliased images from all channels, a set of R pixels of the underlying image can be solved from the above equation. The entire image can be solved by forming a similar equation at all spatial locations in the aliased image.

An example is given in Fig. 2.4. Here the receive sensitivities of the two-channel array are given in (a). The underlying image to be reconstructed is shown in (b). The sensitivity modulated received channel images are given in (c) and the aliased channel images are in (d).

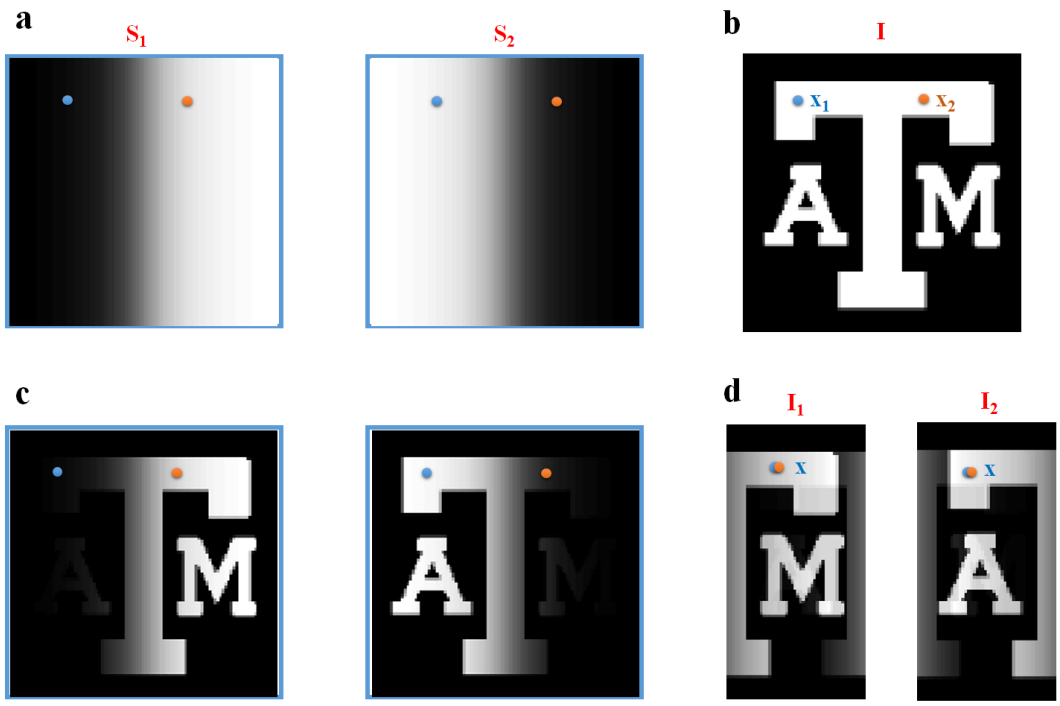

Figure 2.4: Example of SENSE reconstruction

The SENSE formula for a position x in the aliased images can be written as,

$$\begin{pmatrix} I_1(x) \\ I_2(x) \end{pmatrix} = \begin{pmatrix} S_1(x_1) & S_1(x_2) \\ S_2(x_1) & S_2(x_2) \end{pmatrix} \begin{pmatrix} I(x_1) \\ I(x_2) \end{pmatrix} \tag{2.4}$$

then the value of the underlying image I at location x_1, x_2 can be solved. To solve the entire image I, a large equation of this kind that contains all pixel values in the aliased images can be set up and the solution is I.

This SENSE formula is for 2D imaging on Cartesian grid with accelerated acquisition in the phase encoding direction. And it can be simply extended into multi-dimensions with more accelerated phase encodings.

SENSE as other parallel imaging method, is applicable on MRI scanners with re-

ceive arrays when reducing imaging time is more critical and the degradation of SNR can be tolerated. Generally, SNR will reduce by the square root of the acceleration factor.

Unlike conventional MRI, the receive sensitivity maps B_1^- of the coils are necessary in SENSE reconstruction process. Some methods to acquire sensitivity such as simulation using Biot-Savart law, measurement of uniform phantom image at the same position are not accurate due to the loading effect. Or a combination of coil array and body coil can be used and sensitivity is obtained by image division. In the proposed method, full FOV image at the target slice is obtained and sensitivity is obtained by division of individual image by sum-of-square reconstruction. But this requires additional imaging time which may dispel the benefit of parallel imaging. So how to rapidly obtain accurate sensitivity information is of great concern for the SENSE method.

Also, although the SENSE method is not restricted to Cartesian sampling pattern, the computation cost for solving a non-Cartesian SENSE problem may be tremendous as fast Fourier transform cannot be used. Usually, it will be solved using iterative methods such as conjugate gradient with griddings as in [35]. The SENSE method has been implemented on Philips Commercial scanners. And this method can be fitted into already installed system without changes in system hardware.

2.2.2 PILS

The PILS method [18] can be used for partial parallel imaging when the sensitivity coverage of the coils in the array are localized. This is equivalent to reduced FOV for individual channels. After the under sampling, aliasing will not cause the individual image content to overlap each other. Thus, the image can be recovered by cutting out the proper part of each channel and combine them together.

The drawback of PILS is that the acceleration depends on the geometry of the coils and the sampling scheme is limited on the Cartesian. Another problem of the PILS method is that the cutting location is selected as the peak of the sensitivity map which is not optimal. This is discussed in Section 4. Also, the final reconstruction is a spatial combination of individual cut images with low SNR similar the SMASH method.

2.2.3 SMASH: Simultaneous Acquisition of Spatial Harmonics

The SMASH method [43] is the first proposed k-domain parallel imaging method. It manipulates the receive sensitivities of coils in array to synthesize spatial harmonics and therefore some Fourier encodings steps can be skipped to save data acquisition time.

Suppose all the coils in a linear array have spatially varying receive sensitivities along the array direction y and are uniform in the other direction x. Let the coil sensitivity is denoted by $C_j(x, y)$ for the j-th channel. The assumption is that by linear combinations, coil sensitivities can form a Fourier harmonic of spatial frequency $m\Delta k_x$ using complex valued weight as given in Eq. 2.5,

$$\sum_j n_j C_j(x, y) = C^{comp}(x, y) = \exp\left(i \cdot m\Delta k_y \cdot y\right) \tag{2.5}$$

From the data acquisition in MRI, we know that given a phase encoding at k_y, the acquired data by the j-th channel is,

$$S_j(k_x, k_y) = \iint C_j(x, y) I(x, y) \exp\left(-i(k_x x + k_y y)\right) dxdy \tag{2.6}$$

where $I(x, y)$ is the underlining image determined by proton density and imaging parameters. If we form a linear combination of the acquired data from multiple coils

using the same coefficients as in Eq. 2.5, the synthesized data is

$$\begin{aligned} & S^{comp}(k_x, k_y) \\ &= \sum_j n_j \iint C_j(x,y) I(x,y) \exp\left[-i(k_x x + k_y y)\right] dxdy \\ &= \iint I(x,y) \left(\sum_j n_j C_j(x,y) \right) \exp\left[-i(k_x x + k_y y)\right] dxdy \\ &= \iint I(x,y) C^{comp}(x,y) \exp\left[-i(k_x x + k_y y)\right] dxdy \end{aligned} \tag{2.7}$$

Plug Eq. 2.5 into Eq. 2.7, we have

$$S^{comp}(k_x, k_y) = \iint I(x,y) \exp\left\{-i\left[k_x x + (k_y - m\Delta k_y)\, y\right]\right\} dxdy \tag{2.8}$$

This is equivalent to the data acquired with a phase encoding at $k_y - m\Delta k_y$. Thus, by linearly combining the data acquired at k_y from all channels, we can obtain the data at $k_y - m\Delta k_y$. Suppose we can synthesize a total number of M spatial harmonics as in Eq. 2.5, then by applying these coefficients as in Eq. 2.7, we will get all the data at $k_y - m\Delta k_y$ for $m = 1, \cdots, M$ by linear combination of data from all channels at location k_y. And we can acquire one set of data instead of M steps of phase encodings which leads to a factor of M reduction in data acquisition time.

To implement the SMASH method, there are additional requirements and limitations on scanners equipped with receive arrays as listed below.

First, to implement the SMASH method, a linear array is required to generate spatially varying sensitivity in the array direction and uniform in the other direction. This is the only way to provide universal coefficients which will be used to linearly combine the data from multiple channels to form spatial harmonics. Thus, circular

receive arrays may not be used to implement the SMASH method.

Second, although there are no strict limitations on that sampling must be done on the Cartesian grid, the generation of additional spatial harmonics from sensitivities is available only in the array direction. Thus, the accelerated must be performed along the array direction no matter which original full sampling scheme is used. This makes it difficult to be used in trajectories such as spiral and radial.

Finally, similar to the SENSE method, the receive sensitivities of the receive array are required as pre-knowledge for the SMASH method in order to obtain the optimal combination coefficients. The performance greatly depends on the accuracy of coil sensitivity measurement. Errors in sensitivity estimation will lead to severe aliasing artifact due to the incorrectly synthesized spatial harmonics.

2.2.4 AUTO-SMASH and VD-AUTO-SMASH

The SMASH method requires the information of the coil receive sensitivity B_1^+ to calibrate the weighting coefficients. There are two following up methods that do not need the B_1^+ receive sensitivity: the AUTO-SMASH method [24] and the VD-AUTO-SMASH [21]. The idea is similar to the training process in pattern recognition. These methods introduce the concept of auto-calibration signals (ACS) which are just some additional data acquired comparing to the original SMASH sampling scheme at central k-space. And the weighting coefficients can be estimated using these signals without measuring the reception sensitivities. ACS are usually acquired in the central k-space for higher SNR. They are also included in the final reconstruction to further reducing the aliasing artifacts. The only drawback is that the actual acceleration benefit of pMRI is degraded because of these additional acquired data.

The sampling schemes of these three methods are shown in Fig. 2.5. Note that all these three methods are combining down-sampled date from multiple channels to

obtain a single fully sample data. The k-space data are combined by direct sum for these three methods in most cases in the calibration step and in the final combination of acquired data. This can lead to phase error and lower SNR comparing to sum of square image combination.

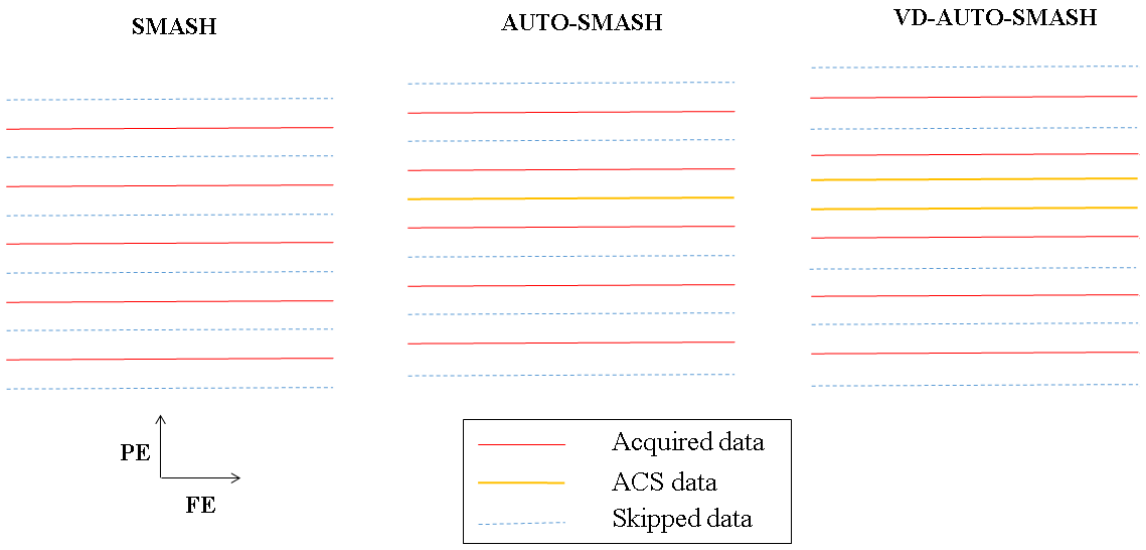

Figure 2.5: The sampling schemes of the SMASH method, the AUTO-SMASH method and the VD-AUTO-SMASH method

2.2.5 GRAPPA and MCMLI

The k-domain parallel MRI reconstruction methods such as Generalized Auto-calibrating Partially Parallel Acquisition (GRAPPA) or (Multicolumn Multi-line Interpolation (MCMLI) are developed based on the above methods. The difference is that the k-space missing data of each individual channel are reconstructed instead of a single composite one. Similar ACS data is acquired and used for calibrating the interpolation weights. GRAPPA employs a reconstruction kernel that covers only the FE direction while the MCMLI method uses a kenerl covering both the FE and

PE directions.

Here is the formulation of the MCMLI method. Let $S(k_y, k_x)$ be the acquired k-space data where y is in the PE dimension, and $\Delta k_y, \Delta k_x$ be the sampling intervals along k_x and k_y axis, respectively. The proposed reconstruction algorithm can be represented as,

$$S_j\left(k_y + r\Delta k_y, k_x\right) = \sum_{l=1}^{C} \sum_{b=-N_b}^{N_b} \sum_{h=-H_l}^{H_r} W_{j,r}\left(l, b, h\right) \times S_l\left(k_y + br\Delta k_y, k_x + h\Delta k_x\right) \tag{2.9}$$

where j and l are the channel indices, C is the total number of channels, R is the acceleration factor, and $r = 1, ..., R-1$ is the relative location of current data point being interpolated. N_b is the number of neighbour blocks along the PE dimension and H_l, H_r are number of neighbour columns used on left and right side, respectively. $W_{j,r}$ is the interpolation coefficients of the r-th net coefficients to target channel j. Here the interpolation kernel is rectangular with varying size. This interpolation formula for arbitrary channel is written in matrix form as,

$$\mathbf{S}_{target} = \mathbf{S}_{source}\mathbf{W}_r, r = 1, ..., R-1 \tag{2.10}$$

where $\mathbf{W}_r$ is the coefficient vector of length $C \times 2N_b \times (H_l + H_r)$, $\mathbf{S}_{target}$ represents the data to be reconstruced or the ACS data and $\mathbf{S}_{source}$ represents the acquired data. In the first step, in the fully sampled ACS area, $\mathbf{W}_r$ is obtained as $\mathbf{W}_r = \mathbf{S}_{source}^{-1}\mathbf{S}_{target}$ when the $\mathbf{S}_{target}$ is known as the ACS data. Then, the obtained weights is can be used to reconstruct the missing k-space data for this channel at the r-th relative location when $\mathbf{S}_{target}$ is the unknown missing data using Eq. 2.10. The sampling

scheme and the reconstruction procedure is shown in Fig. 2.6.

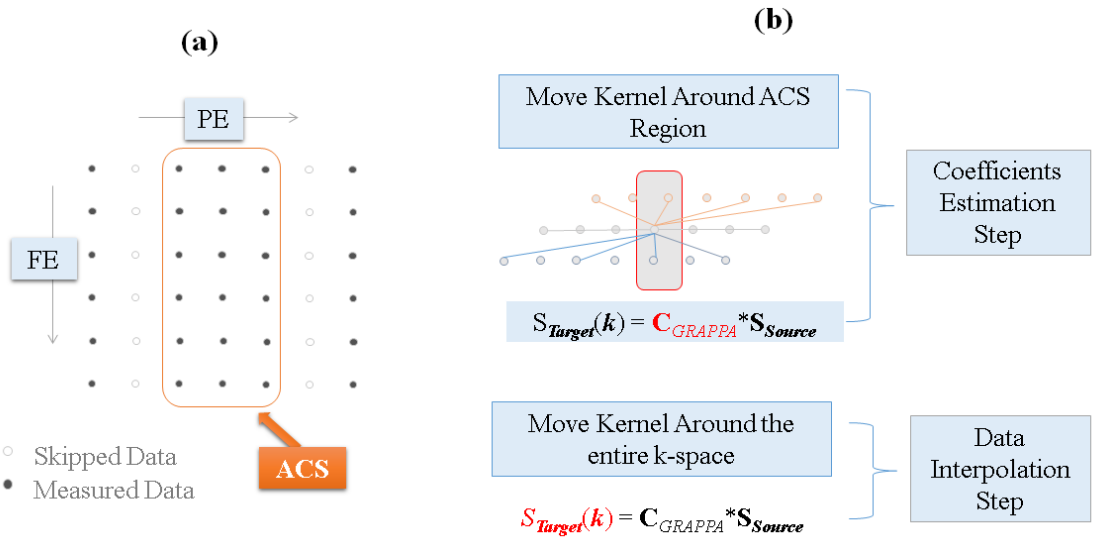

Figure 2.6: (a) The sampling scheme of GRAPPA, central k-space is not down-sampled and used as ACS (b) the two reconstruction steps: calibrate interpolation coefficients and interpolate the whole k-space

Comparing to the SMASH kind of methods, GRAPPA and MCMLI enjoy the SNR benefit from serveral perspectives. First, the ACS works only as training data in the SMASH method. But in GRAPPA and MCMLI, the ACS data from each individual channel are also kept in the final reconstruction. So the ACS are always chosen at the central k-space to achieve minimal aliasing power in the reconstruction and highest SNR for coefficients calibration. Also, instead of reconstruct a single set of final k-space data as in the SMASH method, the GRAPPA and MCMLI reconstruct all the individual channel data and the final image is obtained by sum of squares combination with increased SNR.

2.2.6 Validations

In all simulation of parallel imaging methods, we had acquired the fully sampled data set. The data is pseudo-sampled to mimic the accelerated sampling of parallel imaging and reconstruction is performed. The sum of squares of the fully sampled data is taken as a ground true reference to evaluate the reconstruction results.

The limitation of pseudo-sampling is that only Cartesian sampling scheme is allowed and the acceleration factor has to be an integer.

2.2.7 Efficiency Concerns in Parallel Imaging

PI methods can accelerate data acquisition by collecting less data. The k-domain method is an important and most popular class of PI methods. Unlike most of spatial domain methods, the reception coil sensitivities B_1^- (which may require additional scans) are not required in k-domain methods and the reconstruction is more stable. However, there are other efficiency concerns in k-domain methods.

The first concern is the reconstruction computation cost for k-domain PI methods. The k-domain methods interpolates missing k-space data with a kernel. The kernel usually covers both the imaging dimensions (frequency encoding and phase encodings) and the coil dimension. Coefficients of the kernel are estimated from additional acquired ACS data. When the number of elements in an array increases, computation cost of image reconstruction can increase dramatically. This problem can be even challenging when large arrays with a huge number of element coils are used.

The other concern is the actually acceleration achieved by the k-domain method. Although more ACS data can increase the calibration accuracy of the interpolation coefficients and provide reconstructions with lower aliasing power, it also degrades the actual achieved acceleration factor which defines the ratio of the amount of actual

acquired data to the size of full data. It is always desirable to minimize the size of ACS with similar reconstruction quality.

While trying to address these efficiency concerns, we want the other reconstruction performance related factors to be kept at the same level if not improved. For example, the reconstruction accuracy and SNR in reconstructions.

2.3 Parallel Excitation

The field strength of the current clinical scanners are advancing to 3 Tesla or even 7 Tesla which can tremendously improve the imaging quality. However, many high field related problems remain unsolved, for example, the B_1 inhomogeneity and the high specific absorption rate. The implementation of spatial tailored pulses in combination with parallel excitation provides a promising way to solve these problems.

Unlike traditional Sinc pulses which are generally used for slice selection, spatial tailored pulses with time varying excitation gradient are able to selectively excite arbitrary 2D or 3D spatial shapes, for example, to counter the inhomogeneous B_1 field. The spatial tailored pulses are generally longer than traditional slice selection pulses.

As a signal transmission analogy of parallel imaging, parallel excitation employs the extra degree of freedom offered by multiple transmit channels and curtails the length of pulses. Thus, parallel excitation can be used to reduce the length of spatial tailored pulses to acceptable length or reduce the RF deposition power. Many parallel excitation pulse design techniques had be proposed during the past decade [26, 48, 16].

In this section, the spatial domain method is introduced first in detail. An example of a single channel spatial tailored pulse design is given using the spatial domain method. And the simulation validations and experimental validations are provided.

The computation efficient of this pulse design method is then discussed.

2.3.1 Spatial Tailored Pulse Design Using the Spatial Domain Method

We will first briefly review the conventional spatial domain method [16] for spatial tailored pulse design with parallel excitation.

Under small tip angle assumption (STA) [33], the excitation pattern of transverse magnetization and the complex RF pulse are Fourier pairs defined on the chosen k-space trajectory. Parallel excitation pattern of a multi-channel transmit system is the linear sum of the excitation patterns from all the channels weighted by the transmit sensitivity of each individual coil,

$$M\left(\vec{x}\right) = i\gamma M_0 \sum_l S_l\left(\vec{x}\right) \int_0^T b_l(t) e^{i\vec{x}\vec{k}(t,T)} dt \tag{2.11}$$

where $M\left(\vec{x}\right)$ is the specified spatial target patter, S_l is the B_1^+ map of the $l-$th channel and the excitation trajectory is defined as integral of gradient $\vec{k}\left(t,T\right) = -\gamma \int_t^T G(s)ds$. To solve the RF pulse $b_l(t)$, Eq. 2.11 is discretized in time and in space as shown in Eq. 2.12 and its matrix form as in Eq. 2.13,

$$M\left[\vec{x}_i\right] = i\gamma M_0 \sum_l S_l\left[\vec{x}_i\right] \left(\sum_j b_l\left[t_j\right] e^{i\vec{x}_i\vec{k}[t_j]} \right) \tag{2.12}$$

$$\mathbf{m} = \sum_l \mathbf{S}_l \mathbf{A} \mathbf{b}_l \tag{2.13}$$

where $\mathbf{m}$ is the vector form target pattern, $\mathbf{S}_l$ is the sensitivity matrix of the l-th channel with the constant $i\gamma M_0$, $\mathbf{A}$ is the inverse Fourier encoding matrix defined on the k-space trajectory $\vec{k}$, and $\mathbf{b}_l$ is the sampled driving RF waveform vector of the l-th channel to be solved. Bold variables denote the matrices and vectors.

Then the pulse design problem can be formulated as a minimization problem,

$$\min \|\mathbf{m} - \mathbf{S}\mathbf{A}_{full}\mathbf{b}\|_2 \tag{2.14}$$

where the system matrix is defined as $\mathbf{A}_{full} = \sum_l \mathbf{S}_l\mathbf{A}$ and the $\mathbf{b}$ vector is a stack of $\mathbf{b}_l$ from all the channels. Then numerical methods such as conjugate gradient method (CG) can be used to solve the problem.

2.3.2 Pulse Design Validations via Bloch Simulator

As the spatial domain method is based on the small tip angle approximation, the actual excited pattern would be different from the target pattern. In simulations, we use the so called Bloch simulator to evaluate the excitation pattern of a given pulse. In the Bloch simulator, the RF pulse and gradient are approximated by a serial of hard pulse which is constant valued during the dwell time interval δt. In real experiments, both the RF pulse and the gradient are sampled as a serial of hard pulses. Thus, the Bloch simulator provides a very accurate match between the simulation and the experiment. In the Bloch simulator, all the B_1 fields including the gradient field and the RF pulses (can be multi-channel) are combined by vector sum. Each hard pulse produces a nutation and procession on the magnetization vector and this rotation can be represented by a unitary rotation matrix in SU(2) form using the forward SLR transform[32]. The rotation angle for the j-th hard pulse is given by

$$\phi_j\left(\vec{x}, t_j\right) = -\gamma\Delta t\sqrt{\left|B_{1,x}(t_j)\right|^2 + \left|B_{1,y}(t_j)\right|^2 + \left(\vec{G}(t_j)\cdot\vec{x}\right)^2} \tag{2.15}$$

and the rotation axis for the j-th hard pulse is given by

$$\vec{n}_j\left(\vec{x}, t_j\right) = \frac{\gamma\Delta t}{|\phi_j|}\left(B_{1,x}(t_j), B_{1,y}(t_j), \vec{G}(t_j)\cdot\vec{x}\right) \tag{2.16}$$

where Δt is the dwell time, $B_{1,x}$ and $B_{1,y}$ are the x-direction and y-direction component of the RF pulse, $\vec{G}$ is the gradient vector and $\vec{x}$ is the spatial location vector.

After aggregating all the rotations from the entire pulse via multiplication of each individual rotation matrix, the net effect of the pulse on the magnetization vector comes out as a total rotation. And the excitation pattern can be obtained by calculating the projection of the final magnetization vector onto the transverse plane.

In case that there is spatial varying off-resonance $\Delta B_0(\vec{x})$ during the excitation and Eq. 2.15 and Eq. 2.16 are modified by replacing the z-component of the total field $\vec{G}(t_j) \cdot \vec{x}$ with $\vec{G}(t_j) \cdot \vec{x} + \Delta B_0(\vec{x})$. In some experiments, pulses are designed with consideration of the off-resonance and this off-resonance should be included in the Bloch simulator.

An pulse design and Bloch simulation example is given here. The spatial domain method is used to design a spatial tailored pulse that targets to excite the Texas A&M University logo pattern as shown in Fig. 2.7(a) with a 20cm FOX. The pulse is designed for a single channel birdcage coil with uniform B_1^+ map using Eq. 2.14 while the $\mathbf{S}$ is a Identity matrix. A spiral-in trajectory as in Fig. 2.7(b) is used. The designed pulse is given in Fig. 2.7(c).

Given the gradient and this designed pulse, the Bloch simulator can be used to evaluate the excitation pattern at arbitrary spatial range and resolution by specifying the desired spatial vector $\vec{x}$. Two patterns obtained using the Bloch simulation with different observing scales are provided in Fig. 2.8 and Fig. 2.9. Since the FOX is set to 20cm in the pulse design, the outer region is taken as 'don't care' region with serious excitation artifact.

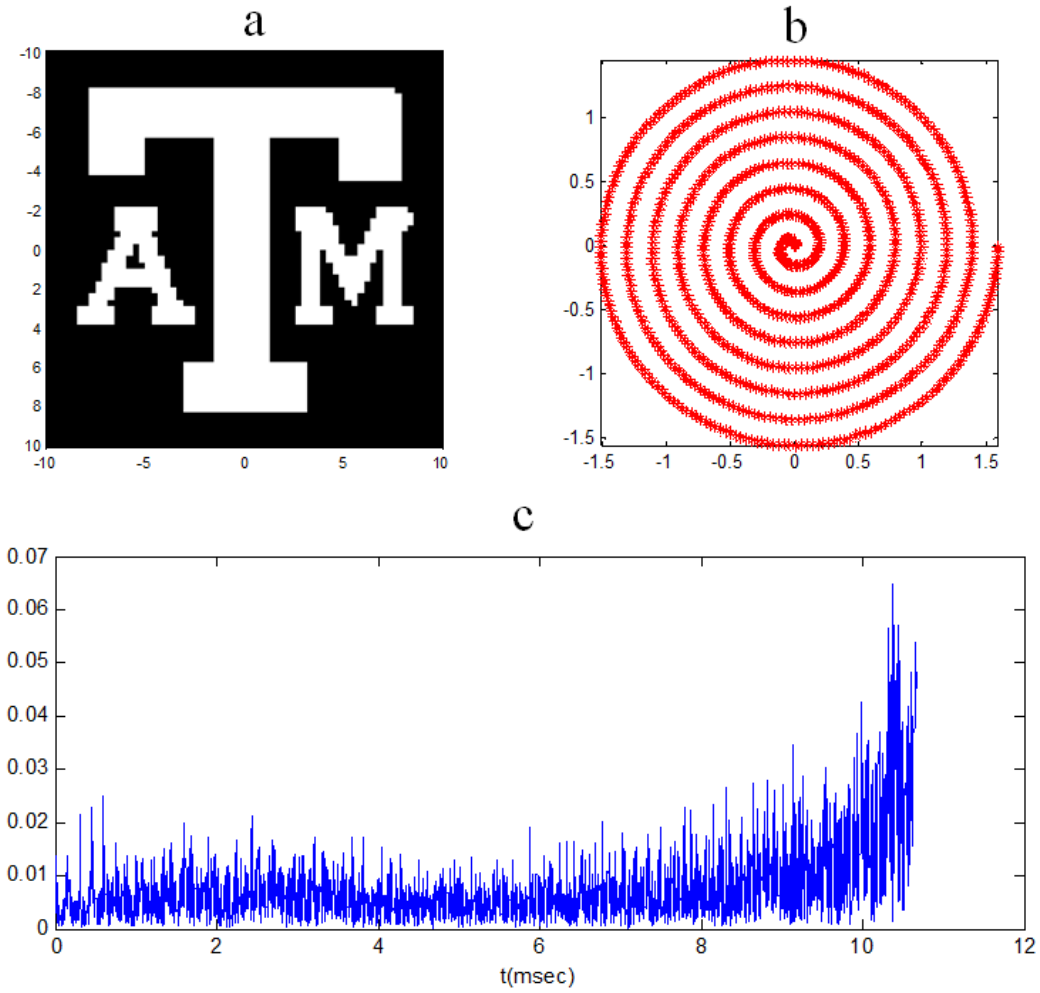

Figure 2.7: (a) The target excitation logo pattern (b) the spiral-in trajectory and (c) the designed pulse

2.3.3 Pulse Design Validations via Experiments

In the previous section, the Bloch simulator has been introduced. It had been used to evaluate the excitation pattern of a single channel RF pulse or multiple channel RF pulses in all the simulations.

In this section, we will prove the reliability of the Bloch simulator by scanner experiments. A single channel RF pulse aiming to achieve a complex valued target

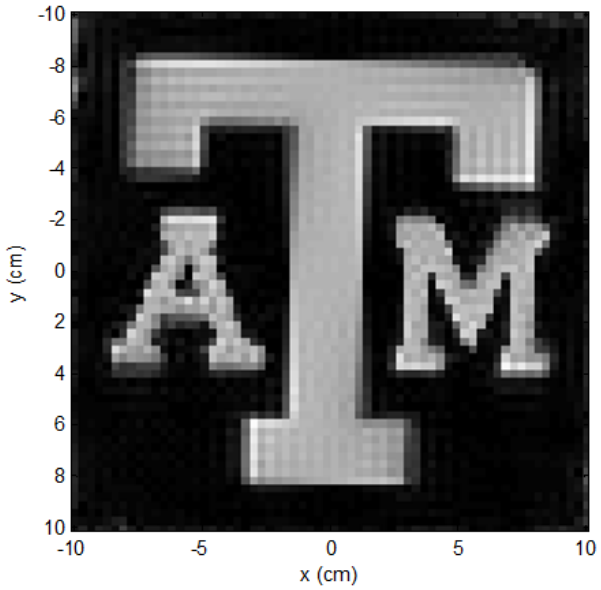

Figure 2.8: Excitation pattern from the Bloch simulator on a 20cm grid

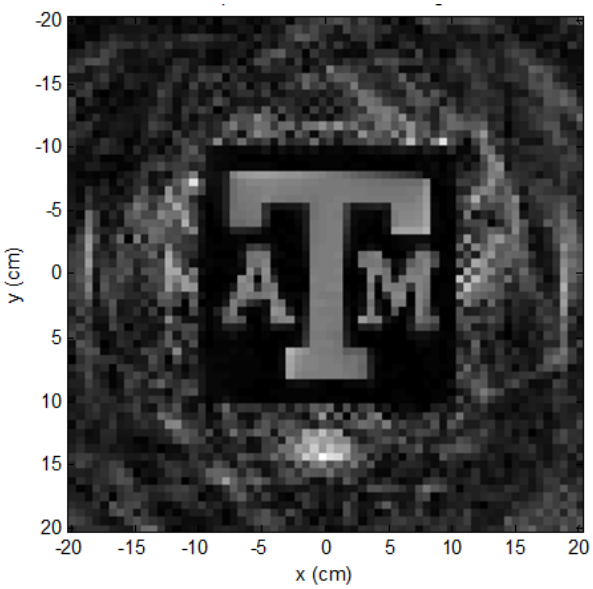

Figure 2.9: Excitation pattern from the Bloch simulator on a 40cm grid

pattern is designed using the spatial domain method. The excitation pattern is evaluated with the Bloch simulator and the experimental scans. The results are

then compared to check if they match. Although this is a single channel test, the excitation magnetic field generated by multiple channel pulses is the linear vector sum of individual pulses. So is the multiple channel excitation pattern which equals to the linear summation of individual patterns. Thus, the demonstration of the effectiveness of the Bloch simulator for the single channel case can be sufficiently generalized to multiple channel cases. Meanwhile, the target pattern to be achieved is complex valued and the reliability of the Bloch simulator can be generalized to multiple channel cases with arbitrary complex valued B_1^+ maps.

The experiments are performed in the Magnetic Resonance System Lab (MRSL) at Texas A&M University on a 4.7 Tesla small core MRI scanner. A cylinder phantom with diameter of 7cm is filled with water and used for imaging. A single birdcage coil tight to the cylinder surface is used for both the RF excitation and signal reception. Typical spin-echo (SE) pulse sequence is used to acquire the phantom image as shown in Fig. 2.10.The following imaging parameters are used through out all the experiments: 35/2000 msec TE/TR, 80mm$\times$80mm FOV, 256×64 (FE$\times$PE) readout matrix. The acquired image is expected to be the complex valued excitation pattern since a uniform water phantom is used for imaging.

To implement the designed spatial tailored pulse, a modified SE sequence is used. The first 90° pulse is replaced by the designed spatial tailored RF pulse. At the same time, the gradient for spiral trajectory is applied in the in-slice plane without slice selection gradient.

Two complex target patterns are specified with square magnitude (1 inside and 0 outside) and linear phase as shown in Fig. 2.11. The linear phase directions of these two target patterns are flipped in the horizontal direction. Two pulses are designed using the spatial domain method with a disk region of interest (ROI) mask. Spiral-in k-space trajectory is used without acceleration and the pulse length is about 10 msec.

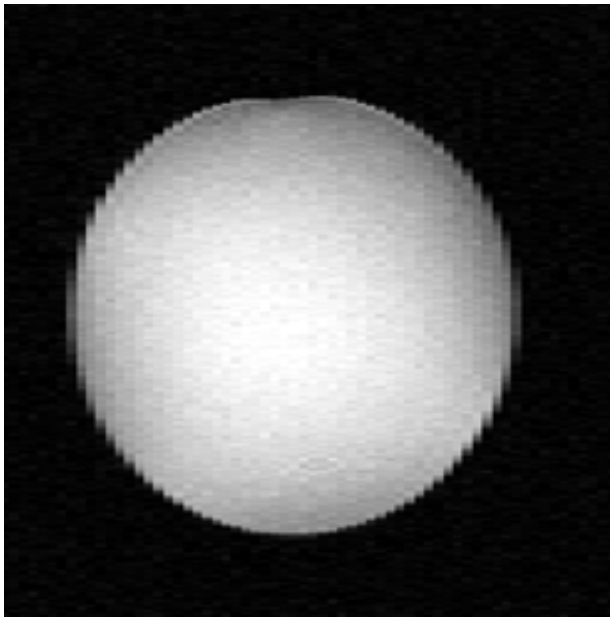

Figure 2.10: Water phantom

The Bloch simulator results for these two pulses are shown in Fig. 2.12. Both the magnitude patterns and the phase patterns are the same as specified in the design. Then, the pulses are tested on the scanner with the same setup as stated above. The acquired image are shown in Fig. 2.13. Since the water phantom is uniform, the contrast in the acquired images are purely from the RF excitation and the acquired images can be taken as excitation patterns. The magnitude image is used as a mask on the phase image (rectangular marked line). As shown, both the magnitude patterns and the phase patterns are consistent with the simulation results except for the slight clockwise rotation and the size is a little larger than the simulation pattern. The rotation is led by a relative delay between the gradient and the RF pulse in the hardware and can be corrected with calibration scans. The relative size difference between the simulation pattern and the experiment image is the result of the mismatch between the FOX in pulse design (10cm) and the FOV in acquisition

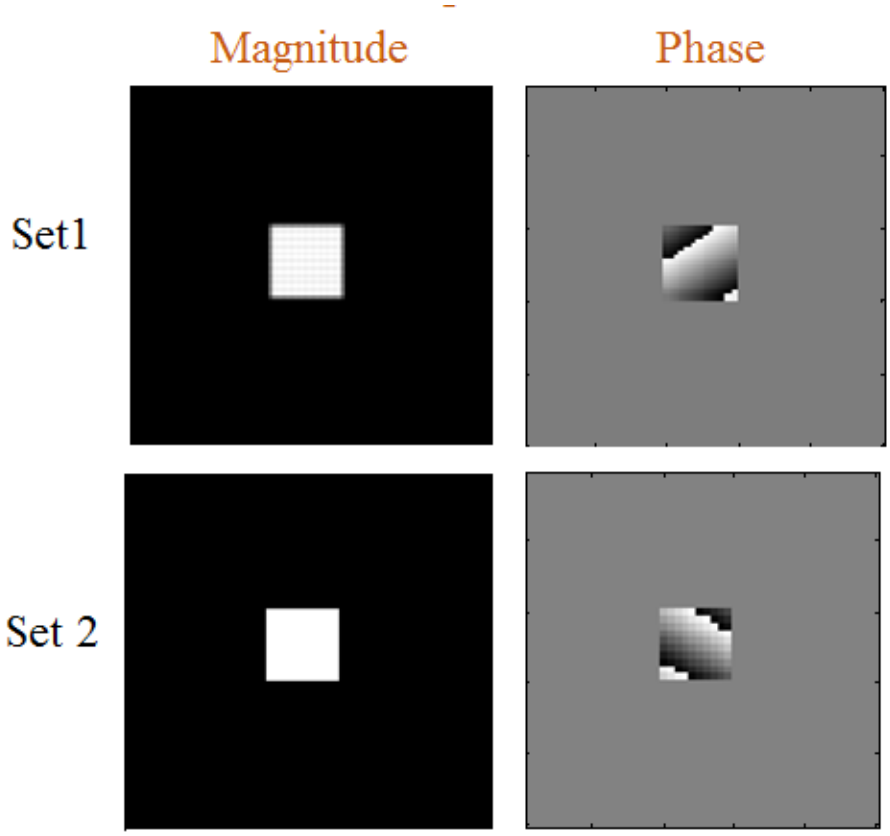

Figure 2.11: The complex target patterns

(8cm).

In this section, the simulation results have been proved to be consistent with the experimental results. Although this validation is for single channel pulse design, in multi-channel case, both the RF pulses and the excitation patterns follow the linear rule and are summations of individual ones. In multiple channel pTx pulse designs, individual excitation pattern are usually complex due to the complex B_1^+ map. The target patterns used in this section are complex valued and provide a general example. In the other pulse design sections in this dissertation, only the Bloch simulation results are provided to evaluate the performance of the designed pulses.

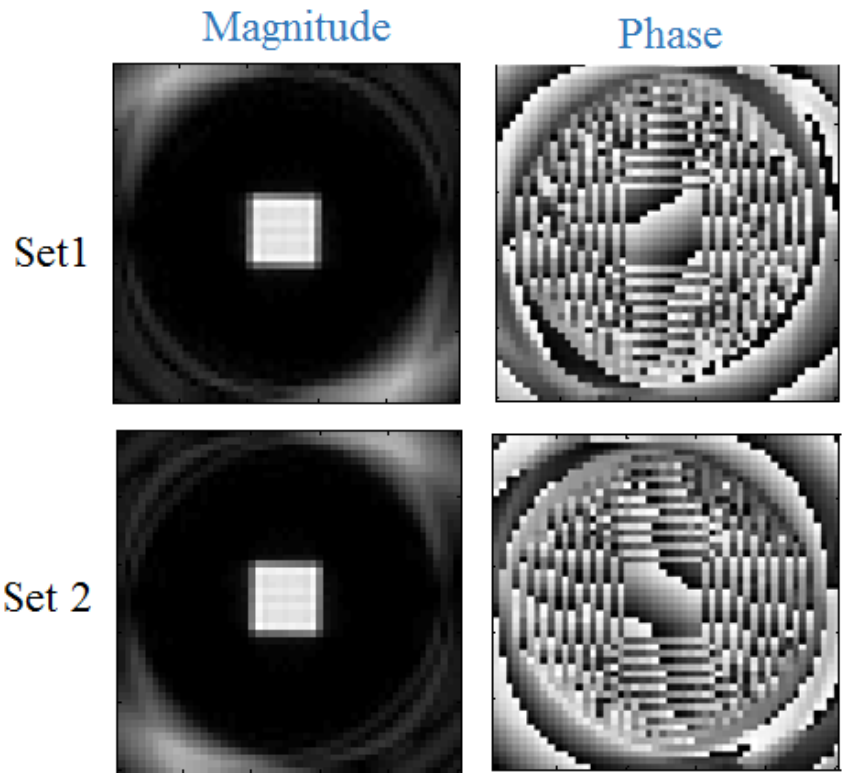

Figure 2.12: The excitation patterns from the Bloch simulator

2.3.4 Efficiency Concerns in Parallel Excitation

The spatial domain method discretizes the Bloch equation under STA and transforms the pulse design problem into a minimization problem of a linear equation. Conjugate gradient method provides a relative fast way to solve this problem. However, the computation cost can be high depending the size of design grid and the amount of iterations.

For example, in a typical 2D pulse design with 8-ch transmit array, designing a 9 msec pulse to excite a target pattern specified on a 50×50 grid will take around 40 sec using CG for 100 iterations. And the computation load increases linearly with the number of channels, the resolution of the target pattern, the number of iterations

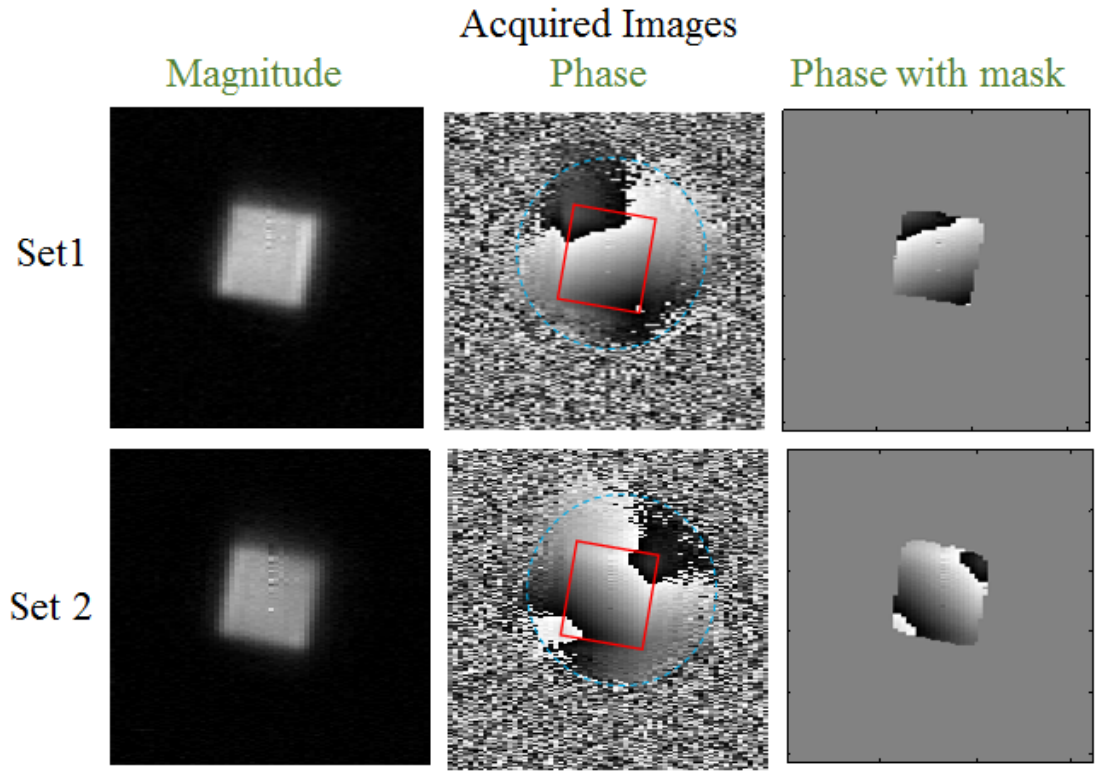

Figure 2.13: The acquired images from the experiments: magnitude image (1st column) is used to mask the phase image (2nd column) to get the masked phase image (3rd column)

and the length of pulse length. This hinders the real time application of pulse designs in clinical usage. Meanwhile, to storage the system matrix $\mathbf{A}_full$, the above example requires around 500 MB memory space. This matrix may have multiple copies in the CG such as its complex transpose. So the required memory can easily exceed the available memory of a PC when the design problem increases to a larger scale.

General-purpose graphics processing unit (GPGPU) has been used to accelerate the pulse design process [7]. In this work, the complex matrix-vector multiplication which is the most computation expensive part in CG is splited as 4 real matrix-vector multiplications and distributed to 4 GPUs for parallel computation. 20 fold

acceleration has been proved comparing to the CPU of similar price range. However, the available memory on GPUs is 1G to 2G at acceptable price. A pulse design on large scale can be hard to be implemented with GPU.

In a word, the efficiency concerns in pulse design using the spatial domain method includes the computation speed and the memory cost.

3. K-DOMAIN PARALLEL MRI USING CHANNEL-BY-CHANNEL ARRAY REDUCTION *

3.1 Introduction

In the past two decades, parallel imaging (PI) using array coils and multi-channel receiver has experienced rapid advance from basic technological development to a range of clinical applications. Although conventional receiver arrays are usually limited to less than 16 channels, a particular exciting trend in this area is the development and application of massive receive arrays with 32 or more parallel channels [31, 28, 19]. By virtue of using a high number of parallel channels, massive array has enormous potential to provide highly parallel high-speed MRI.

One pressing problem in this exciting area is data processing efficiency. Because both the data volume and processing complexity increase with the number of channels, computational burden becomes very significant as the massive array system is used to acquire data [47]. This is particularly challenging for real-time applications such as in cardiac MRI.

Interestingly, most literatures on massive array PI use SENSE reconstruction [28, 19, 36] or SEA reconstruction [3]. Autocalibrating k-domain parallel MRI such as the GRAPPA (Generalized Autocalibrating Partially Parallel Acquisitions) methods, which are widely used in PI with conventional arrays, are rarely applied to large array systems [21, 17]. Because k-domain PI involves channel-by-channel calibration and reconstruction, the computation time generally increases nonlinearly and at a rate

*Reprinted with permission from "Efficient large-array k-domain parallel MRI using channel-by-channel array reduction" by Shuo Feng, 2011. Magnetic Resonance Imaging, Volume 29, Issue 2, 209-215, Copyright [2011] by Elsevier

faster than image-domain methods. Specifically, because the interpolation model in GRAPPA uses a multi-dimensional kernel that spans across phase encoding direction, frequency encoding direction, and the coil direction, model calibration in GRAPPA involves pseudo inversion of very large matrices whose complexity is on the order of $O(N^3)$. Therefore, improving the efficiency of k-domain reconstruction for massive array can lead to wider applications of the k-domain methods and utilize the full potential of massive arrays.

To achieve improved data processing efficiency in the large array systems, software compression (linear combination of channel data prior to reconstruction) or channel reduction (selecting a small set of most important channels) have been proposed [8, 5, 22]. For SENSE, the sensitivity matrix can be truncated, or the coil set can be reduced to a smaller size using singular value decomposition [8]. However, with these methods the efficiency has to be achieved with somewhat reduced reconstruction quality, for example, reduced SNR. Some existing methods could also in principle be applied to large array k-domain PI, for example, the method that obtains the optimal kernel by decomposing a larger kernel using the singular vectors [37]. However, computing the singular vectors is not trivial computationally. For massive arrays with large number of elements, an important insight is that as the size of coil element trends to be small, its sensitivity is quite localized. Therefore in interpolating the missing k-space data for a particular channel, only a subset of "neighbouring" channels in the whole array system is necessary. This fact can be used to reduce the interpolation kernel size and consequently the computation cost in k-domain PI with massive arrays, as originally proposed in [44] and recently further reported in [13, 20, 40, 9].

In this work, an efficient reconstruction method is proposed for k-domain parallel MRI with large arrays using array reduction. The process of selecting reduced

channel set for GRAPPA kernel is based on the cross-channel correlation using the calibration data inherent in GRAPPA reconstructions. The proposed algorithm was tested using both computer simulations and real MRI data acquired from phantoms and in-vivo studies using a 64-channel and 32-channel system, respectively. The effect of array and signal reduction is studied in terms of efficiency, artifact, and SNR. The experimental results show that the proposed method using reduced kernel can achieve a reconstruction quality almost the same as that of a kernel which contains all channels, but with significantly reduced reconstruction time.

3.2 Theory

3.2.1 K-domain PI Reconstruction with Channel Reduction

With massive arrays, the sensitivity of an individual channel is localized compared to FOV. Therefore, data from each channel contains information of only a small part of the FOV. Two channels that are spatially distant may provide little information of each other and interpolating one with the data from the other has no benefit. An example of massive array of linear distributed coils with localized sensitivity is given in Fig.3.1. The figure shows the 1-D profiles of the channel sensitivities. As shown, in order to interpolate the channel in the center (bold solid line), only the neighbour channels (bold dashed lines) are needed. Other channels provide no or little relevant information. Because the coefficient vector has a length proportional to the number of total channels, using all channels in reconstruction may lead to large computation cost for massive array. Hence, channel reduction is necessary to reduce reconstruction errors and accelerate computation. This can be achieved by utilizing the locality of channel sensitivity.

The idea is to keep only a small set of neighbour channels which are correlated with the channel being reconstructed. All irrelevant channels with little desired infor-

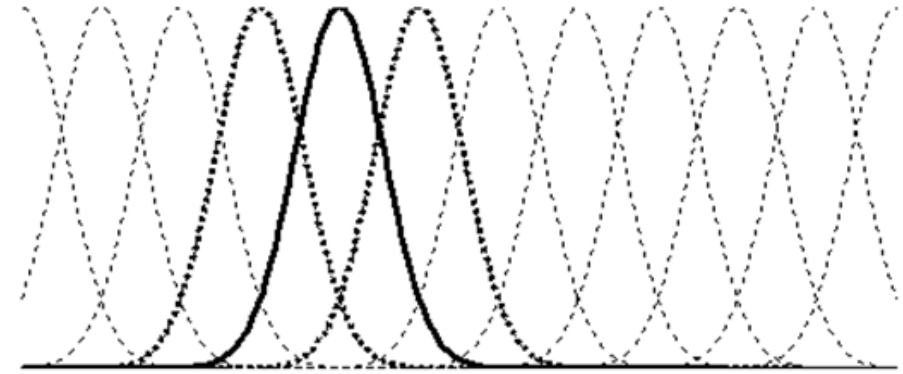

Figure 3.1: One-dimensional profile of coil sensitivities in a large coil array with localized sensitivity

mation are dropped from the interpolation model for the channel. The reconstruction using this reduced set of channels is expected to achieve the same or improved quality as using all channels. The MCMLI reconstruction formula is modifed from Eq. 2.9 as below.

$$S_j\left(k_y + r\Delta k_y, k_x\right) = \sum_{l \in C_i} \sum_{b=-N_b}^{N_b} \sum_{h=-H_l}^{H_r} W_{j,r}\left(l, b, h\right) \times S_l\left(k_y + br\Delta k_y, k_x + h\Delta k_x\right) \tag{3.1}$$

where j and l are the channel indices, R is the acceleration factor, and $r = 1, ..., R-1$ is the relative location of current data point being interpolated. N_b is the number of neighbour blocks along the PE dimension and H_l, H_r are number of neighbour columns used on left and right side, respectively. $W_{j,r}$ is the interpolation coefficients of the r-th net coefficients to target channel j. In the proposed algorithm, C_j represents the set of channels that will be used to interpolate the data in the j^{th} channel. Note that due to the localized element sensitivity in large arrays, C_j

only includes a subset of all channels which contains relevant information for the j^{th} channel.

Obviously, efficiency gain is expected to be achieved using the proposed method. Assume that on average N_c channels were selected for each channel after channel reduction, the total computation and memory complexity will be reduced by a factor of $O\left(\left(\frac{N_c}{C}\right)^p\right)$ where C is the total number of channels and P is a power number depending on whether direct matrix inversion or conjugate gradient method is used to calculate the interpolation coefficients. The N_c selected channels should be determined by channel sensitivity on the image plane. For example, in Fig.3.1 the selection can be made by simply choosing neighbour channels of a target channel based on sensitivity overlap. In more general cases such as non-linear arrays, a more rigorous method is required to make selection automatically.

3.2.2 Channel Selection Using the Correlation Information

In this paper, channel correlation is used for this purpose. Correlation is a metric that measures the relevance of two signals. Stronger correlation between two channels generously indicates more overlap of their sensitivity coverage and carrying more similar spatial information of each other. Specifically, channel correlation coefficient, as a special case of Eq.12-2-8 in [14], between the m^{th} and the n^{th} channels is computed using,

$$\rho\left(m,n\right)=\frac{\mathrm{cov}(|I_m|,|I_n|)}{\tau_m\tau_n} \tag{3.2}$$

where $|I_m|$ and $|I_n|$ are the two individual channel magnitude image vectors obtained from the ACS data in the central k-space, τ_m and τ_n are standard deviations of the images. For example, to reconstruct the m-th channel, the reconstructio kernel only

spans the subset of channels given by

$$\cup \{n|\rho(n,m) > \alpha\}$$

The two images are in low-resolution but not aliased. In case of using the aliased image, there can be relative large correlations between the true image from one channel and the aliasing artifact from the other.

In all the studies in this paper, such images provide sufficient correlation information. Note that the metric in Eq. 3.2 is insensitive to channel image intensity or gain. For example, two channels cover the overlapped regions with different gains can be recognized as highly correlated. Therefore, it is superior to the conventional difference metric such as l_1 or l_2 norm. Once a correlation coefficients matrix is obtained, the reconstruction of each channel can be performed using the selected subset of most correlated channels whose are above certain threshold instead of all channels.

This entire reconstruction procedure will be performed off-line using a homemade MATLAB toolbox [25].

3.3 Methods

3.3.1 Computer Simulations

Simulated data was generated using a 64-element linear array of planar pair coils as shown in Fig. 3.2(a). The setup of coil parameters follows a real 64-channel linear array [25]. The slice being imaged is parallel to coil array plane. Channel sensitivity of each channel was calculated according to Biot-Savart equation. K-space data was then obtained from individual coil image which is a standard Shepp-Logan phantom modulated by the generated array sensitivities. Matrix size of sensitivity and the

Shepp-Logan phantom was 256×256. Complex, white Gaussian noise is added to the k-space data.

Three sets of different coil sensitivity were employed as shown in Fig. 3.2(b) to explore the impact of channel selection on the quality of reconstruction results.

Acceleration was simulated by dropping certain lines and filling with zeros along the PE direction which was aligned with array distribution. Thirty-two central PE lines were kept fully sampled as ACS. Channel selection was performed based on correlation matrix before reconstruction. K-space data of each channel was reconstructed using a selected number of $N_c = 3$ to 64 channels. All results were compared with corresponding fully sampled reference.

To measure the signal-to-noise ratio (SNR) of the reconstruction, 30 sets of k-space data were generated for each of the three possible coil sensitivity distributions. After reconstruction, the average of the 30 magnitude reconstructions was taken as signals, and the variance of them was used to measure the noise. Then a 256×256 SNR map was obtained and the average of the SNR map is calculated. In order to measure the reconstruction error associated with different choices of channel numbers, normalized root mean square error (NRMSE) was computed. The sum-of-squares reconstructions from fully-encoded data were taken as ground truth.

3.3.2 2D Phantom and In-vivo Experiments

Fully sampled phantom data with matrix size of 256×256 was acquired using a system of 64-channel linear array on a 4.7 Tesla system [1]. Data along PE direction was decimated by a factor of 2 to simulate GRAPPA data acquisition. Reconstruction of fully sample data was used a reference. A 2-D GRAPPA reconstruction kernel contains 3 neighbor FE points and 2 neighbor blocks were adopted. The ACS size was 40×28 (FE $\times$ PE). It was used for channel correlation computation. Channel

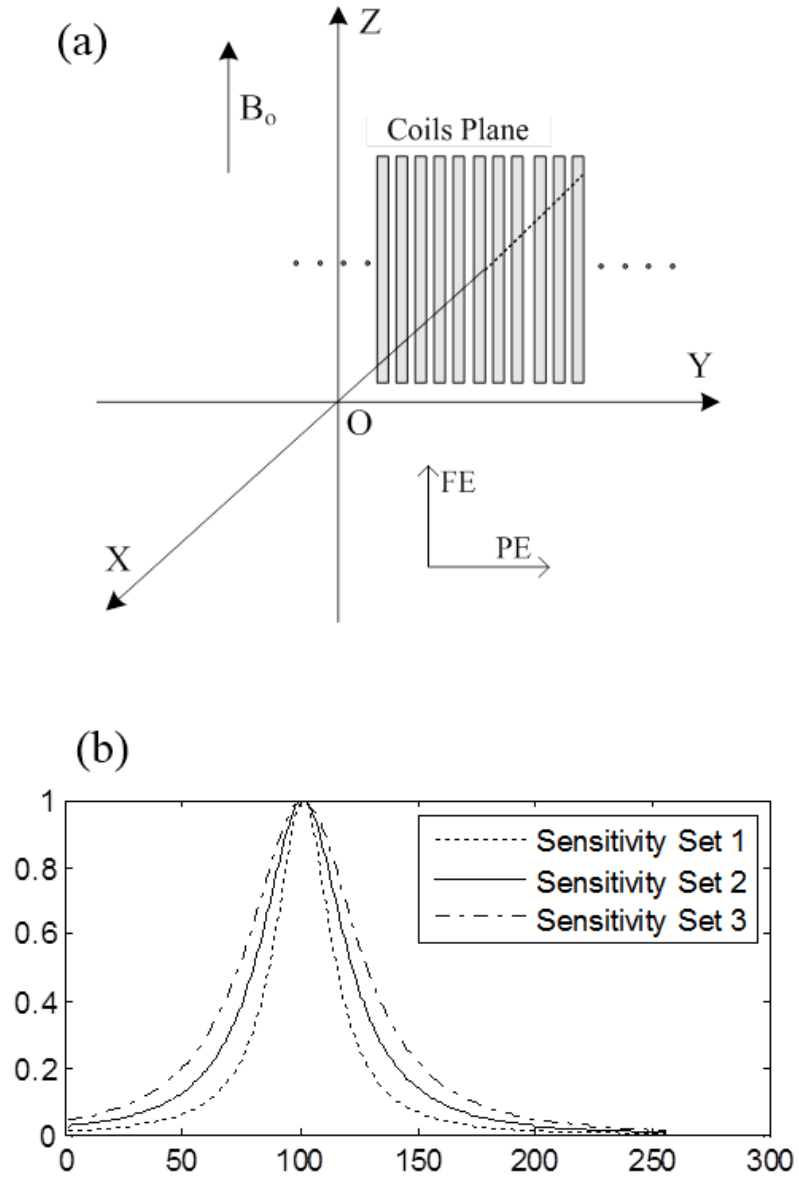

Figure 3.2: Illustration of 64-ch data simulation. (a) The physical layout of the coil array with localized sensitivity and (b) 1-D profile of 3 sets of coil sensitivities

reduction with different numbers was performed at reduction factors of $R = 2$, 4 and 8. Computation time for each reconstruction was recorded to compare computation efficiency. The NRMSE is calculated in a similar way as in the computer simulation using the sum-of-squares reconstruction as a ground truth.

To test the proposed channel reduction theory in case of circular arrays are used, the channel reduction method is implemented on another set of phantom data. The data is acquired using 8-channel circular array. The individual fully sampled image is shown in Fig. 3.3. As can be seen, the channel sensitivity in this array covers a large region within the FOV and all channels have some shared spatial content with the other channels. The channel reduction k-domain method is used to reconstruct the data downsampled at acceleration factor of $R = 2$.

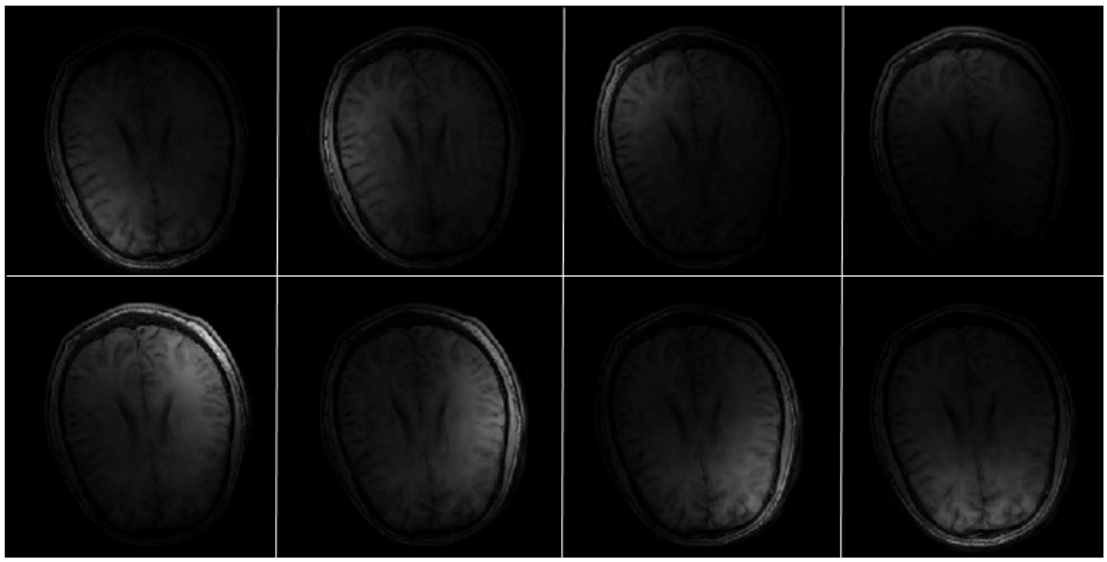

Figure 3.3: Individual channel images acquired using the 8-channel linear array

3.3.3 In-vivo Experiment

Subsampled 3-D *in-vivo* data was acquired from a healthy volunteer using a 32-channel system on a 1.5 Tesla scanner. Reduction factors in both PE directions were 3, resulting in an overall acceleration factor of $R = 9$. ACS size was 28×28 which gives an effective acceleration factor of $R = 6.7$. Reconstruction using the proposed

method was performed with subset of N_c=4, 8, 16 and 32 channels.

3.4 Results

Reconstructions of all 30 sets of simulated data are obtained. One set of results are shown in Fig. 3.4. SNR map is calculated through image series pixel-by-pixel and then average SNR of the SNR map is provided in Table. 3.1. Error image is obtained referring to corresponding fully sampled data and then average NRMSE is given. It shows that using a smaller set of channels, e.g. $N_c = 3$, reconstruction is visually the same as using all channels, i.e. $N_c = 64$, at a reduction factor $R = 2$. Average SNR is at the same level with different number of selected coils. Using all channels is not providing a reconstruction with minimum error.

Table 3.1: SNR vs. different number of selected channels N_c

Number of selected channels	3	31	64
SNR (dB)	33.7	33.4	32.7

Fig.3.5 shows the reconstruction error images from 3 simulated data sets. As shown, as the number of selected channels N_c increases the error reduces rapidly in the beginning. However, above a certain number of N_c, error does not further reduce. This shows that only a small set of selected channels are required in the reconstruction. It also shows that for the cases with wider channel sensitivity, e.g., the 3^{rd} dataset, reconstruction requires more selected channels to arrive at a minimum error level which is lower than cases of sensitivity with smaller coverage. This is expected because the neighbor channels are more correlated as the channel sensitivity becomes less localized.

Results from the phantom data from linear array are shown in Fig.3.6 and 3.7.

Correlation coefficient matrix of the 64-channel images from the acquired ACS data is shown in Fig.3.6. Acceleration factor of $R = 3$ is used and two additional large correlations due to the relative large correlation to aliasing artifact can be observed. For this linear array configuration, significant correlation exists only between close neighbor channels. Therefore, the correlation matrix shows a clear diagonal structure. Reconstructions and error images using $N_c = 7$, 15, 31 and 61 are shown in Fig.3.7. Although adopting some more channels shows a tendency of reduced error, NRMSE is not varying too much in these cases. Reconstruction artifact using all 64 channels is more obvious than other choices as pointed by arrows. To compare the resolution of the reconstructed images with different N_c, 1-D profiles corresponding to a line in the 2-D images along the acceleration direction are shown at the bottom of Fig.3.7. Note that using a small number of selected channels does not lose details in the 1-D profiles.

Computation cost of the reconstruction using different N_c is shown in Fig.3.8. The computation time increases significantly as N_c increases from 3 to 61. For the same N_c, the computation time also increases as reduction factor becomes larger. By performing channel reduction, computational efficiency can be dramatically improved. For example, with $R = 8$ the computation time for in vivo and $N_c = 61$ are 1 minute and 17 minutes, respectively.

The reconstruction results of the data acquired using the circular array is shown in Fig. 3.9. This array has only 8 channels and the individual channel coverage is not that localized in FOV. So as expected, the channel reduction will lead to reconstruction errors and is now feasible in this case.

Reconstructions of *in vivo* data using $N_c = 4$, 8, 16 and 32 are shown in Fig. 3.10. The reconstruction using $N_c = 8$ shows some overall non-uniform intensity, which may indicate that using $N_c = 4$ and 8 are not sufficient. Compared with

reconstruction of $N_c = 16$, reconstruction of $N_c = 32$ shows better contrast but the overall qualities are almost the same. This indicates that using $N_c = 16$ can provide sufficient reconstruction quality with much improved computation efficiency.

3.5 Conclusion and Discussion

In this work, the cross-channel correlation is computed using the low-resolution images from the ACS lines. Alternatively, one can use all the acquired data (ACS + under sampled lines) to obtain channel images for computing correlations. However, it has been observed that this introduced "false" correlation as channel images contain high frequency aliasing which overlaps on other channel's coverage area. The channel selection method proposed in this paper can be viewed as part of a more general optimal kernel selection problem in k-domain parallel imaging. However, this paper focuses on channel reduction only, though in practice the selected blocks, FE columns, channels, acceleration factor, and size of ACS are all important factors that need to be balanced.

An additional benefit of the proposed method is the numerical stability. In GRAPPA and MCMLI, the interpolation coefficients are estimated from ACS using least squares fit solution. Normally, this requires the number of ACS to be larger than the number of unknown coefficients. Note that by performing channel reduction, the number of coefficients is reduced by a factor of $\frac{N_c}{C}$ and thus the required number of samples in ACS is also reduced by the same factor. Therefore choosing ACS size according to size of coefficients can further improve the efficiency with channel reduction.

In conclusion, a method for reducing the computation burden in the k-domain parallel imaging with large receive arrays was presented. By utilizing localized sensitivity, the method adaptively selects a small set of channels in the GRAPPA/MCMLI

interpolation models for each individual channel. Computer simulations and the phantom and *in vivo* studies show that the proposed method can significantly reduce the computational burden while providing comparable reconstruction quality. This offers an additional degree of freedom in k-domain parallel imaging to improve efficiency and quality, which is expected to make these methods more applicable to systems with large receive arrays.

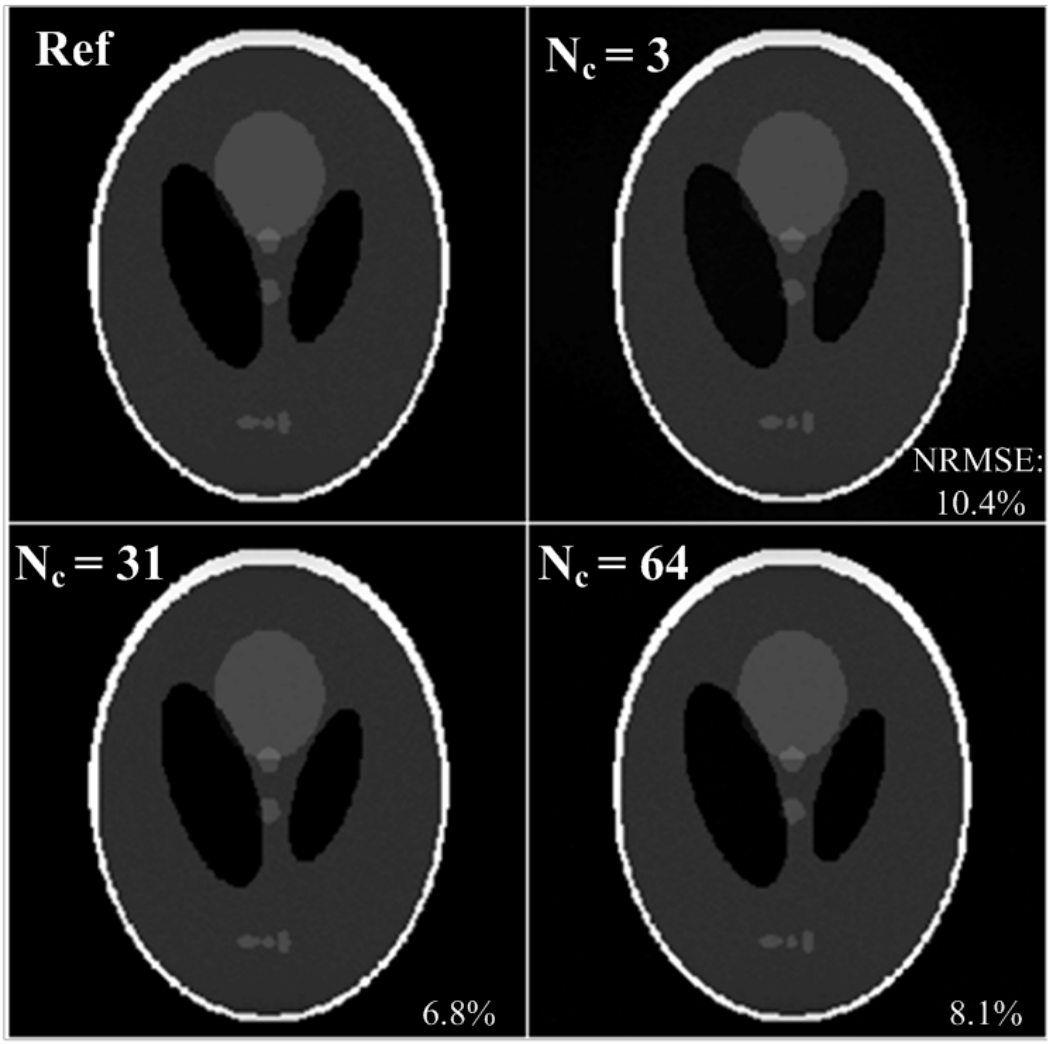

Figure 3.4: Reconstructions from the simulated 64-ch data with different number of selected channels in MCMLI method. Fully sampled image is shown for reference

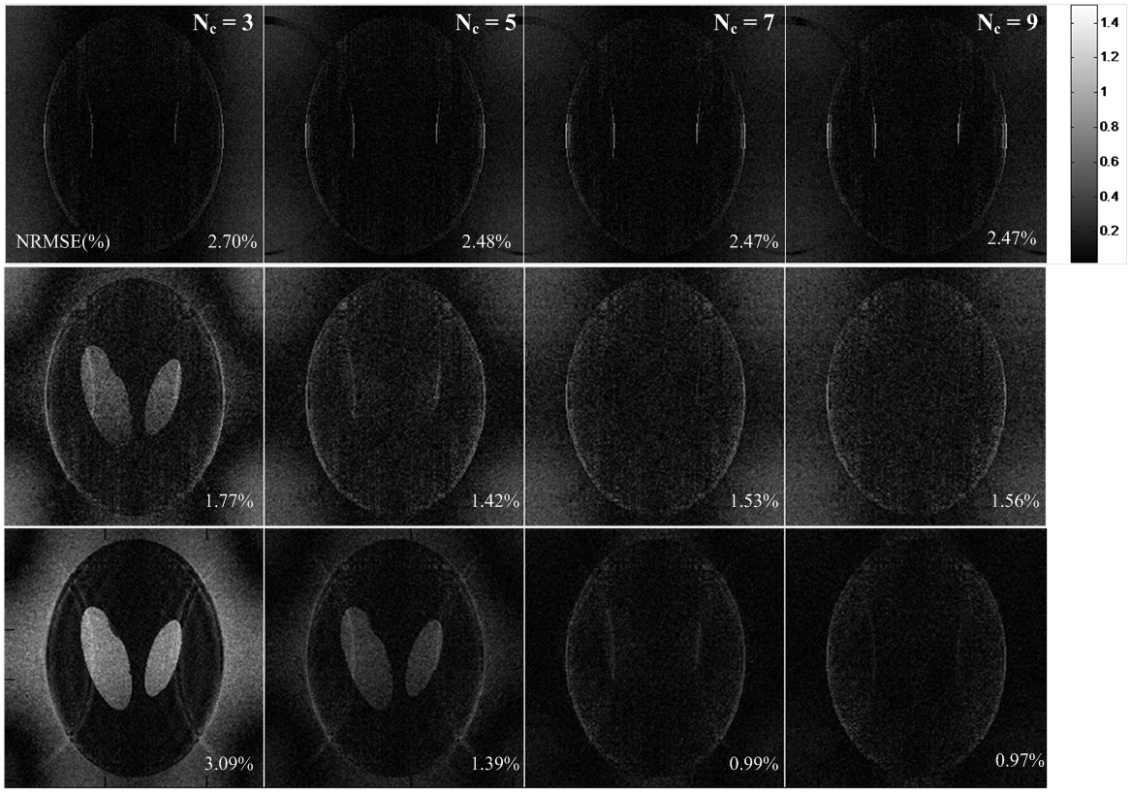

Figure 3.5: Error images using 3 sets of simulated data sets (with narrow, medium and wide sensitivities) with different number of selected channels. Error images of set 1, 2 and 3 are shown in the 1^{st}, 2^{nd} and 3^{rd} rows respectively

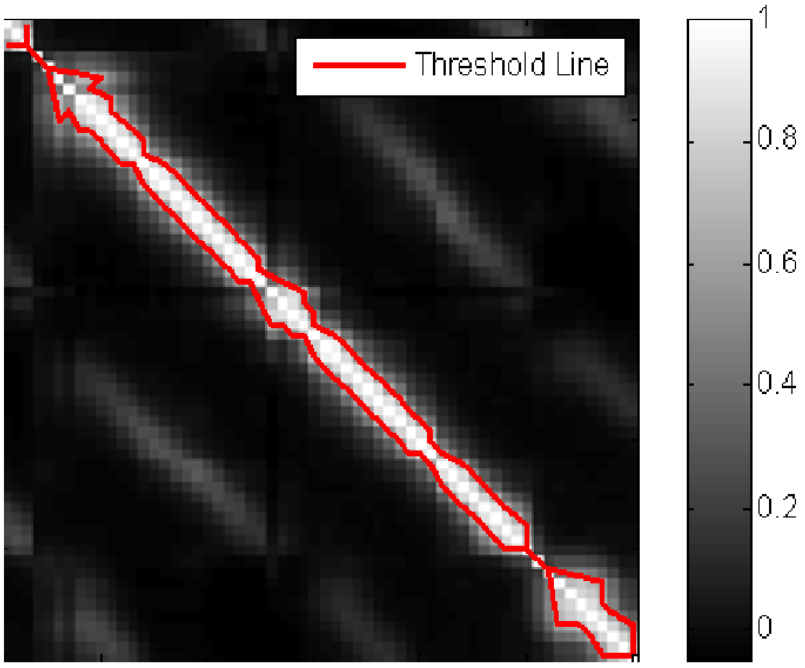

Figure 3.6: Correlation coefficient matrix of a 64-ch receiver system. Significant correlation exists between neighbor channels. Threshold is set at 0.7

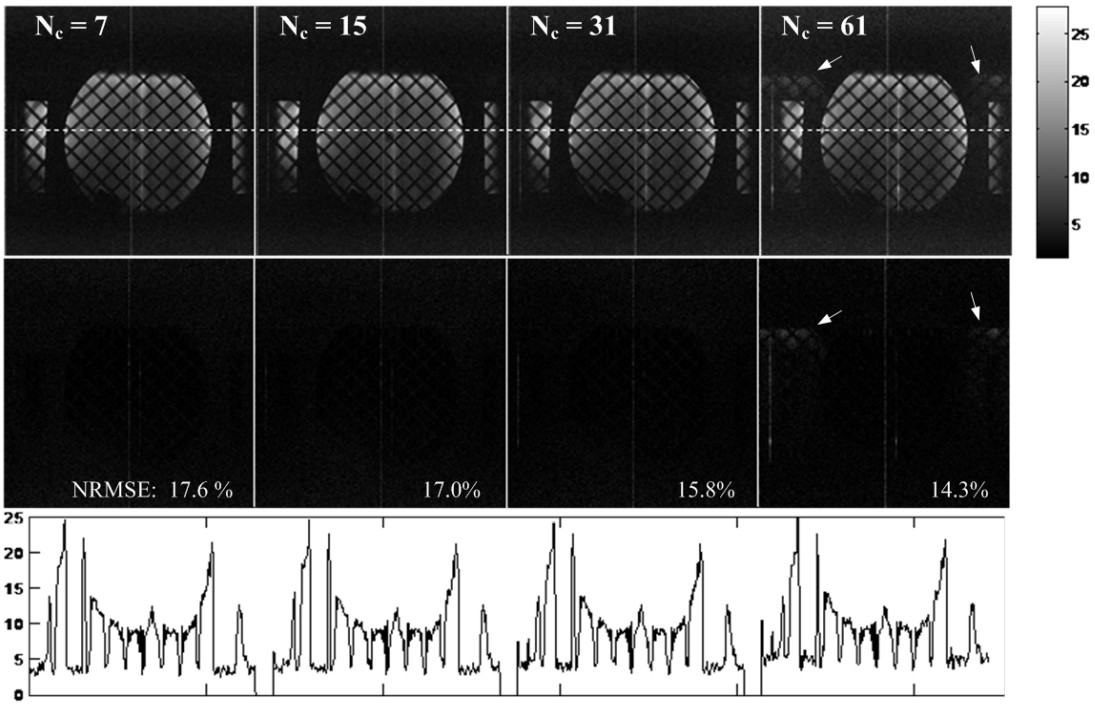

Figure 3.7: Reconstruction results in the 64-channel phantom experiment. Reconstructions (first row) and their corresponding error images (second row) with different selected number of channels ($N_c = 7$, 15, 31 and 61) are shown. A single line (dashed) in each reconstruction is provided to compare resolution. SNR is computed using selected regions shown in the first image

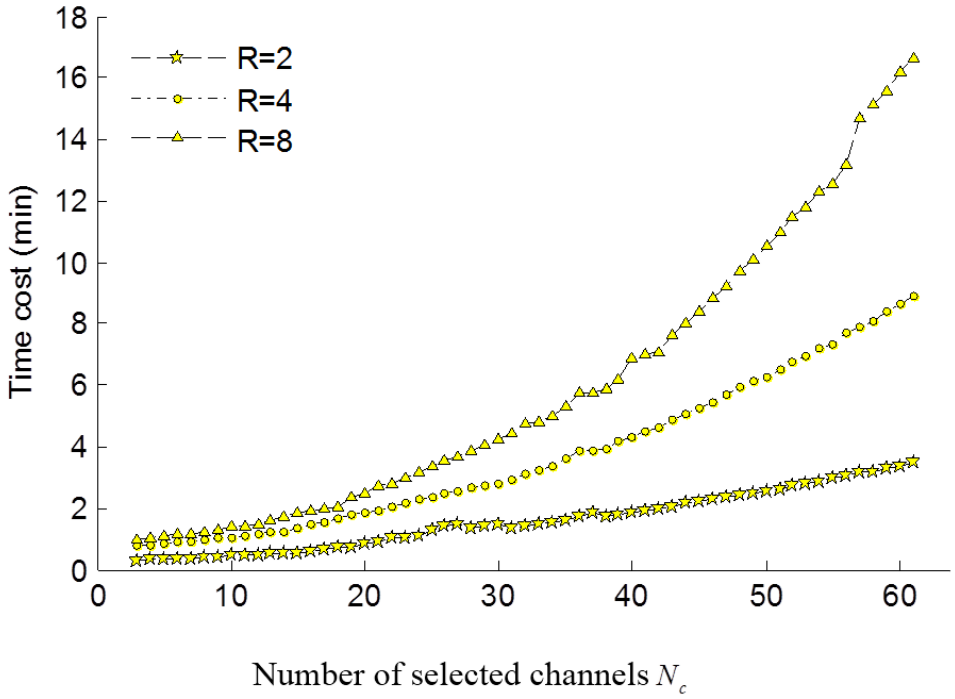

Figure 3.8: Reconstruction time cost versus number of selected channels at different reduction factors

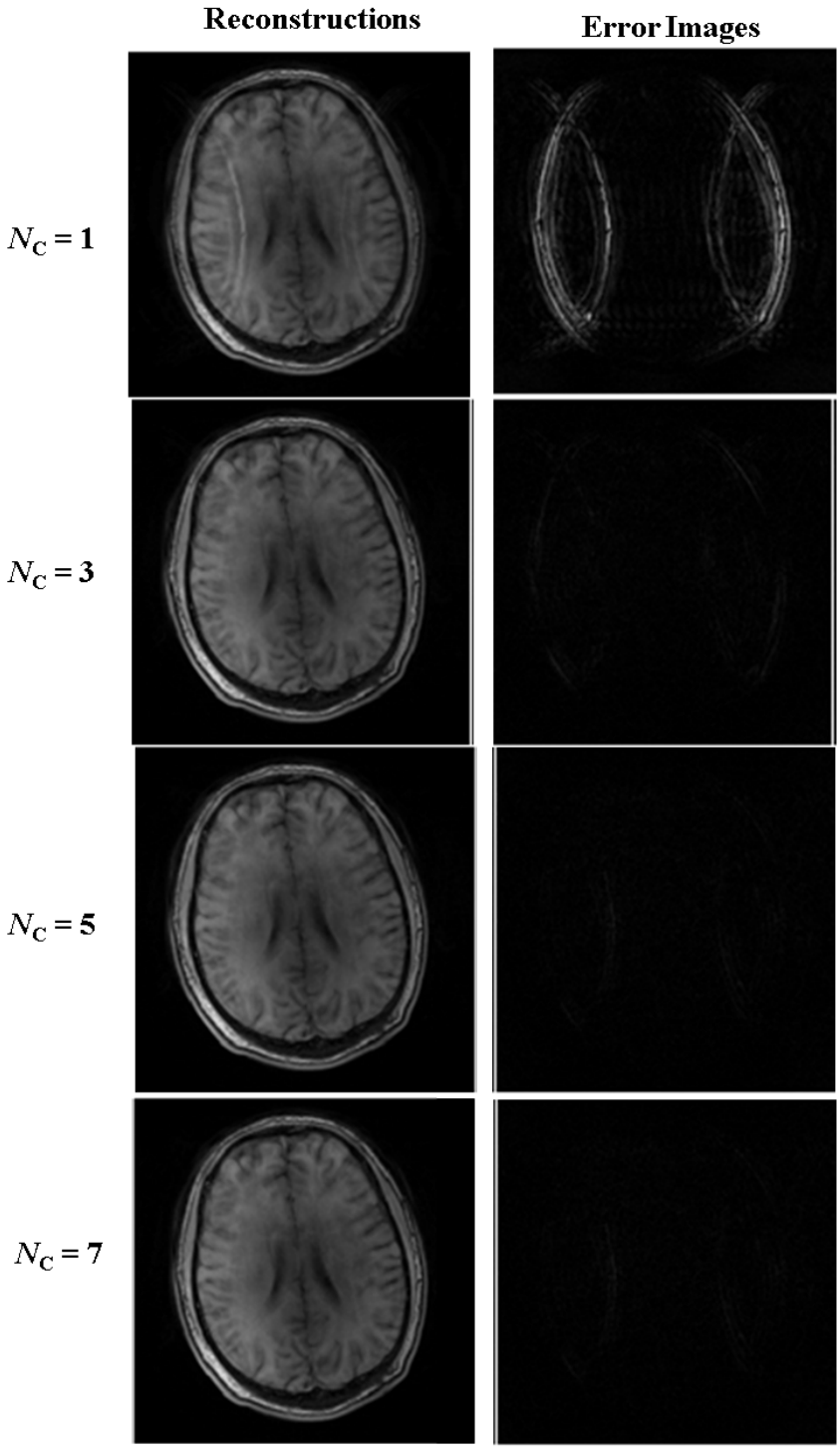

Figure 3.9: Reconstructions of the data acquired using the circular array with different N_c

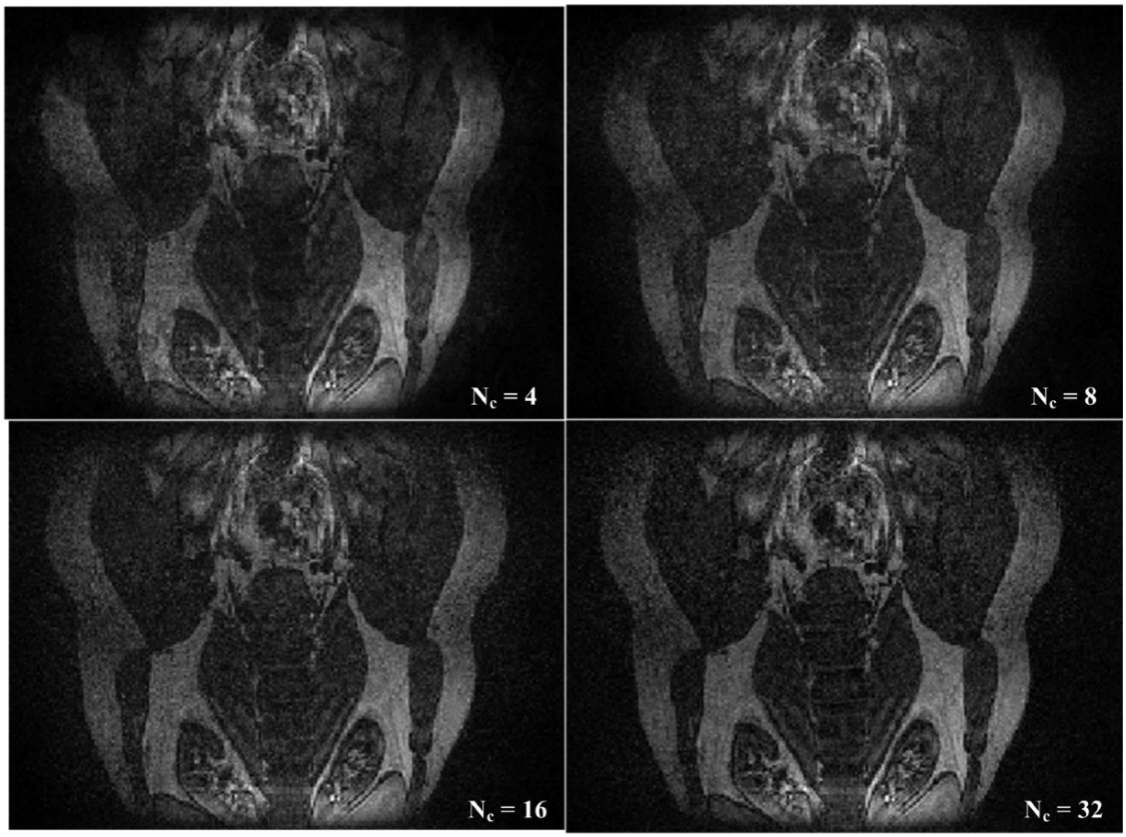

Figure 3.10: Reconstructions of 32-ch *in-vivo* body images with N_c =4, 8, 16 and 32. Only one slice of the 3D image is shown

4. PARALLEL MRI USING LOCALIZED RECEIVE ARRAYS WITH SINC INTERPOLATION (PILARS) *

4.1 Introduction

Parallel imaging (PI) is a technique that can significantly accelerate data acquisition speed with the help of an array of coils, each of which has a unique spatial sensitivity. The underlying sensitivity encoding can help to recover missing data in an accelerated data acquisition process (e.g. skipped phase encoding steps). Some of the PI methods utilize sensitivity directly like SENSE [36], SMASH [43] , SPACE-RIP [27], and PILS [18]. Those methods require a measurement or estimate of receive coil sensitivities to solve an inverse problem. The other methods indirectly employ the effect of spatial encoding by coil sensitivity in a system model. It is assumed that the k-space data are correlated and the missing k-space data can be recovered, for example, by interpolation. Methods of this kind include GRAPPA [17], MCMLI [46, 13], and SPIRiT [29], and are categorized as the k-domain reconstruction methods [4]. The k-space data correlation in these methods come from two sources: (1) inner-channel correlation mainly from the localized coil sensitivity which corresponds to a wide k-space spreading, and (2) inter-channel correlation due to the shared spatial information between receiver coils covering overlapped areas.

As a tendency in MRI coil development, number of coil elements keeps growing and the individual elements become smaller with more localized sensitivities [31, 19, 28]. Thus, optimized reconstruction kernel should be chosen based on sensitivity, as

*Reprinted with permission from "Parallel magnetic resonance imaging using localized receive arrays with sinc interpolation (PILARS)" by Shuo Feng, 2011. Magnetic Resonance in Medicine, Volume 67, Issue 4, 1114-1119, Copyright [2011] by Wiley

has been discussed in [37, 40, 8]. A unique characteristic of large arrays is that the coil sensitivity is highly localized. As a result, the inner-channel data correlation is strong and the inter-channel data correlation is relative weak, as compared to the conventional coil arrays. Therefore the image reconstruction will rely more on inner-channel than inter-channel correlation in larger arrays. In the k-domain PI, this means that the interpolation kernels need to cover a larger k-space area and span fewer overlapped channels [13]. In the image-domain method PILS [18], the inter-channel correlation is completely ignored.

Large arrays, by virtue of the large number of parallel receive channels, are potential to achieve high acceleration factors in the aforementioned methods. However, in practice, the actual achieved acceleration factor is limited by the need for auto calibration signals (ACS) which require additional acquisition time. The size of ACS is proportional to both the acceleration factor and the kernel size. When a large number of ACS has to acquired, the actual acceleration factor is reduced. In this paper, a novel method PILARS that uses pre-determined real Sinc coefficients with complex phase term is proposed. The method uses Sinc kernels for k-space data interpolation that only requires one phase parameter to be estimated using a very small size of ACS. Simulations based on synthetic data and phantom experiments show that the new method can achieve higher actual acceleration factors with improved reconstruction quality comparing to existing k-domain methods. This work is partly developed from previous work [12].

4.2 Theory

4.2.1 PILARS Reconstruction

The basic idea of the method is that for data acquired in PI with large arrays, the skipped phase encoding data can be recovered using a Sinc interpolation. Then

a final reconstruction can be achieved by combining the images from all channels.

Following the Nyquist sampling requirement, k-space sampling interval is determined by desired overall field of view (FOV). Down sampling with an interval larger than the Nyquist interval can lead to aliasing image artifact. In PI, this limit is overcome by the parallel acquisition from channels with different spatial sensitivities. Specifically, it is assumed that individual coil's maximum field of view FOV_c is much smaller than the overall FOV due to its localized sensitivity. Then larger sampling intervals are acceptable in the shrunk direction of FOV_c. Consider a 3D PI case where data is acquired on a Cartesian grid with accelerations in two phase encoding dimensions. In the proposed method, k-space data of a single channel can be recovered by [34],

$$\begin{aligned}\hat{s}\,(m,n) = \sum_p \sum_q s(p,q) \cdot \mathrm{sinc}\left(\frac{\pi}{D_1}(m-p)\right) \\ \cdot \mathrm{sinc}\left(\frac{\pi}{D_2}(n-q)\right) \cdot e^{j2\pi\left(x_0\frac{(m-p)}{M}+y_0\frac{(n-q)}{N}\right)}\end{aligned} \tag{4.1}$$

where $m = 1, 2, ..., M$, $n = 1, 2, ..., N$ are the indices of the recovered signal $\hat{s}$; $p = D_1, 2D_1, ..., M$ and $q = D_2, 2D_2, ..., N$ are the indices of the acquired data s, with acceleration factors D_1 and D_2 along the two dimensions. (x_0, y_0) is the center of a reconstruction rectangular window of size $\left(\frac{FOV_1}{D_1}, \frac{FOV_2}{D_2}\right)$ that covers the area of individual channel image content. This formula employs all acquired k-space data and only one phase term is unknown. Eq. 4.1 is for 3D imaging with two accelerated phase encoding directions where signals along both dimensions are down-sampled. For 2D imaging, or coils with localized sensitivity in only one direction, Eq. 4.1 can be simplified to a 1D Sinc interpolation.

An accurate recovery based on this formula requires an estimate of (x_0, y_0). Note that this center is equivalent to the center of optimal PILARS reconstruction window

rather than coil center. The estimation cannot be obtained from the k-space data acquired with accelerations alone. To find an optimal (x_0, y_0), a few ACS data are acquired. In principle, the number of ACS data points can be as small as two, which are sufficient for estimating the parameters in Eq. 4.1. In this paper, a two-stage phase calibration method is introduced to estimate the parameters, which is described next.

4.2.2 Two-Stage Phase Calibration

To estimate unknown parameter (x_0, y_0), the algorithm first finds an approximate center $(\hat{x}_0, \hat{y}_0)$. Afterward (x_0, y_0) is searched in the vicinity of $(\hat{x}_0, \hat{y}_0)$. In practice, the approximate coil center is located from a profile of the channel image, which is obtained by inverse Fourier transform of the zero-padded k-space data with ACS. Because the higher energy contained in these low frequency harmonics in ACS are not folded, the corresponding channel profile will not be folded and the coil location can be identified directly. A 1-D example is shown in Fig. 4.1. The approximate center $(\hat{x}_0, \hat{y}_0)$ is found at the maximal intensity location along each dimension. Note that in this stage only a rough guess is required.

In the second stage, the optimal window center is chosen by minimizing the error metric based on the ACS, i.e.

$$\min_{(x_0,y_0)} \|\hat{s} - s_{ACS}\|_2 \tag{4.2}$$

where $(x_0, y_0) \in \left(\left[\hat{x}_0 - \frac{M}{D_1}, \hat{x}_0 + \frac{M}{D_1}\right], \left[\hat{y}_0 - \frac{N}{D_2}, \hat{y}_0 + \frac{N}{D_2}\right]\right)$, s_{ACS} is the acquired ACS data and $\hat{s}$ is the interpolated ACS data at the same location using Eq. 4.1 with parameter (x_0, y_0). The minimization is done by exhaustive search. The computation load is low because both the size of ACS and the amount of parameters are small.

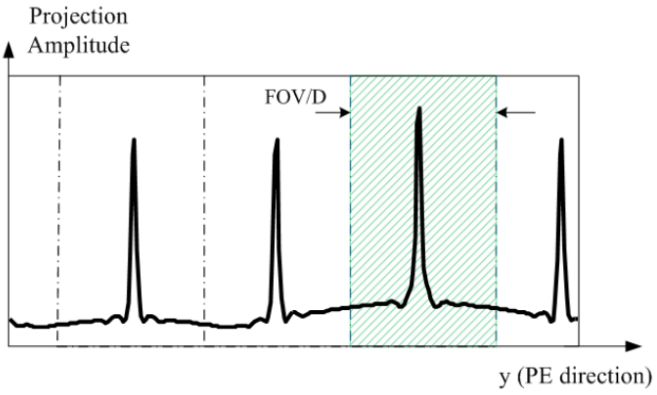

Figure 4.1: Profile of the channel image and localization of optimal center region (shadowed). The profile is obtained from a central k-space line along the horizontal dimension. The maximum of the profile is taken as an initial estimate

4.2.3 Reconstruction Procedure

After the two-stage phase calibration is performed for each channel, Eq. 4.1 is used to interpolate missing k-space data from the acquired data. Channel image is then obtained through inverse Fourier transforming the whole k-space data that includes both the acquired and the interpolated data. A complete single channel reconstruction process is shown in Fig. 4.2. After all channel images are reconstructed, the final image is obtained using the root of sum-of-squares (SOS) method.

4.3 Methods

The proposed method was tested and characterized using computer simulations with both synthetic and real MR data. The simulated data set is from a 36-ch receive array with 2D localized coil sensitivity. Two-dimensional Gaussian function was used to generate coil sensitivity and a 'Shepp-Logan' phantom of size 128×128 was adopted as the target imaging object, which is shown in Fig. 4.3. Accelerated acquisition was simulated by decimation along both directions with a factor of $D_1 =$

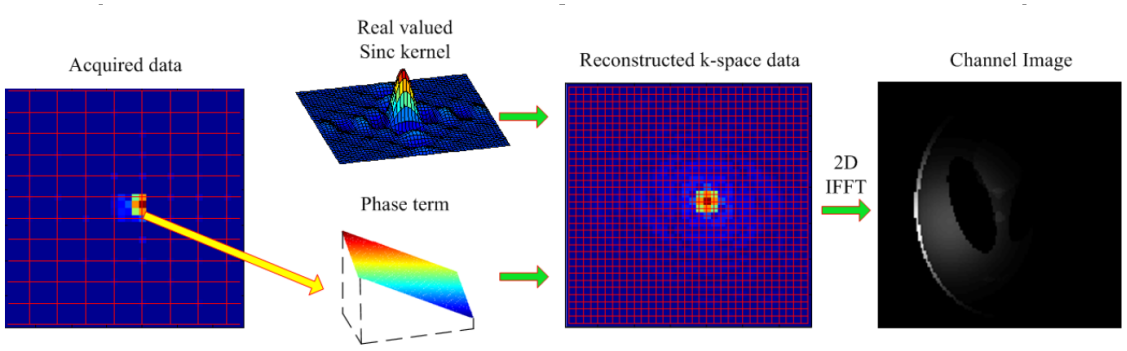

Figure 4.2: Reconstruction process of a single channel in the proposed PILARS method. Eq. (4) is used to recover the k-space data after the phase term is estimated based on ACS

$D_2 = 2$.

Reconstruction from the down-sampled data was performed using the proposed PILARS method, the MCMLI reconstruction, and the conventional PILS method. ACS data in the central k-space with a size of 5×5, 28×28 were used for PILARS and MCMLI, respectively. The PILS method requires an estimate of coil center which should be the maximum amplitude location of the Gaussian function in this case. The PULSAR [25] toolbox was used to perform the PILS reconstruction. The MCMLI method used a reconstruction kernel of size $2 \times 2 \times 36$ (FE-PE-Coil). Reconstruction of the fully sampled data using the SOS method was used as standard reference. Reconstruction errors were calculated as normalized root mean square error (NRMSE). The actual acceleration factor is defined as the ratio of size of fully sampled data to size of actual acquired data:

$$D_{actual} = \frac{MN}{\frac{MN - N_{ACS}}{D_1 D_2} + N_{ACS}} \tag{4.3}$$

where N_{ACS} is the size of ACS, and M, N are the Nyquist number of two phase

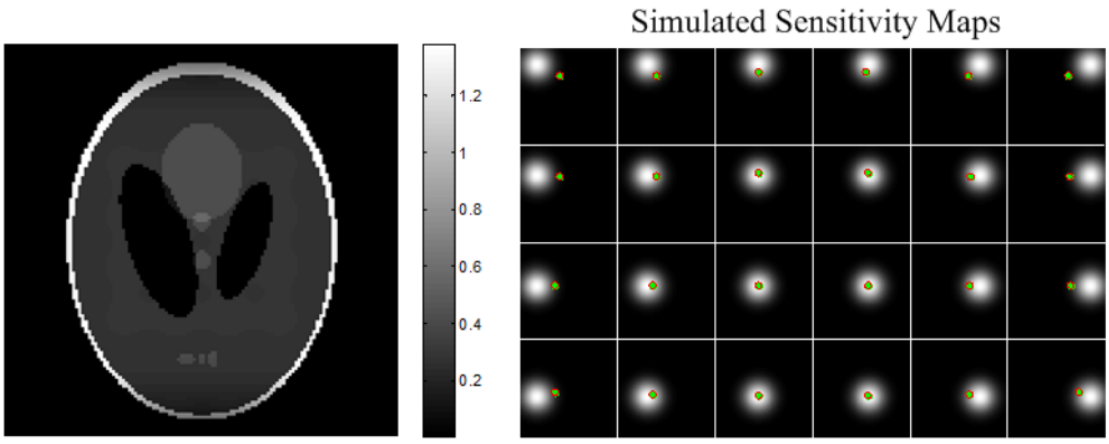

Figure 4.3: The image object and representative coil sensitivities in the computer simulation. Sensitivity maps of the first 24 channels are shown with localization in both directions. Optimal window centers of each channel obtained from the two-stage calibration are shown as dots

encodings. For a more robust calibration, ACS of larger size can be used at the cost of a lower actual acceleration factor.

In addition, a set of fully sampled 256×256 data was acquired on a 4.7T small-bore system using a 64-channel receive coil array. Accelerations were simulated by retrospective decimation of the full dataset. Because the array coils were localized only along the horizontal dimension, acceleration was applied only along that dimension ($D_1 = 1$). Reconstructions using the proposed PILARS method, the MCMLI method and the PILS method with various acceleration factors were performed and compared. A reconstruction kernel of $2 \times 3 \times 3$ [13] was used in the MCMLI reconstruction. And 32 PE lines were used as ACS because it is around the minimum number required for an outer acceleration factor of $D_2 = 10$ with the given kernel size. For the PILARS method, ACS sizes from 2 to 16 were tested. Reconstruction errors were measured using the SOS of full size data as a reference. The actual acceleration factors, reconstruction errors as well as the reconstruction time were

compared for different methods.

All the simulations were performed on a 2.6GHz Dual-core CPU with 2 GB memory in Matlab (Math Works, Natick, MA).

4.4 Results

Coil sensitivities of the first 24 channels in the 36-ch simulated system are shown on the right side of Fig. 4.3. For PILARS method, the optimal window center from the two-stage estimation was obtained for each channel and shown as dots on corresponding sensitivity map. Note that the PILARS optimal center differs from the true coil center which is the position with maximum amplitude of the Gaussian sensitivity. The reconstructed images and the corresponding error images are shown in Fig. 4.4. From the error images and the NRMSE, one can see that the PILARS method yielded minimal reconstruction error. In the MCMLI reconstruction, the errors appear to be more diffused but its actual acceleration factor is smaller. The actual acceleration factors of the three methods are shown on corresponding reconstructions. As shown, the PILARS method achieved an actual acceleration factor very close to $D_1 D_2$ as in the PILS method. The MCMLI method resulted in a smaller actual acceleration factors because it requires a larger ACS size.

Reconstruction results with an outer acceleration factor of 3, 5 and 10 from the real 64-ch data with 1D acceleration are shown in Fig. 4.5 to Fig. 4.7. Acceleration is performed only along the horizontal dimension. Different rows correspond to outer acceleration factors of 3, 5 and 10. The normalized root-mean-square error (NRMSE) is listed in each reconstruction. The actual acceleration factor on corresponding reconstructions. The PILARS method can achieve a similar error level with less acquired data comparing to the MCMLI method. The PILS method presents the largest reconstruction error. The PILARS method and the MCMLI method are also

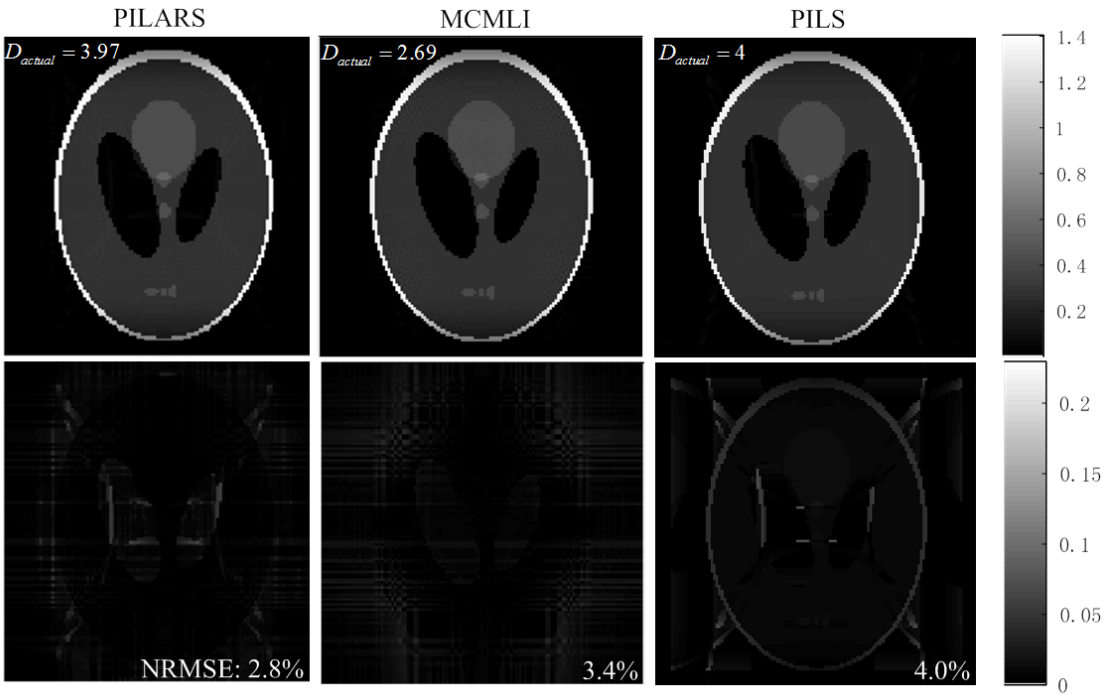

Figure 4.4: Reconstructions from simulated k-space data ($D_1 = D_2 = 2$) using different methods. The bottom row shows the corresponding error images and the quantitative normalized root-mean-square reconstruction error

implemented with an outer acceleration factor of 3 but with different ACS size. The results are shown in Table. 4.1. The NRMSE of PILARS decreases with larger ACS as expected and is much lower than that of the MCMLI method with the same ACS size. Also, the PILARS method can is stable with a small ACS size comparing to the unacceptable reconstruction error of the MCMLI method when ACS is 4 or 8.

The reconstruction time is shown in Table. 4.2. Reconstruction time for the proposed PILARS method is shorter than that of the MCMLI method. As can be seen in Fig. 4.5 to Fig. 4.7 and Table. 4.1, the new method can reach a factor of 6 acceleration with good reconstruction quality. Overall, the proposed PILARS method can reconstruct image with smaller error or provide higher actual acceleration

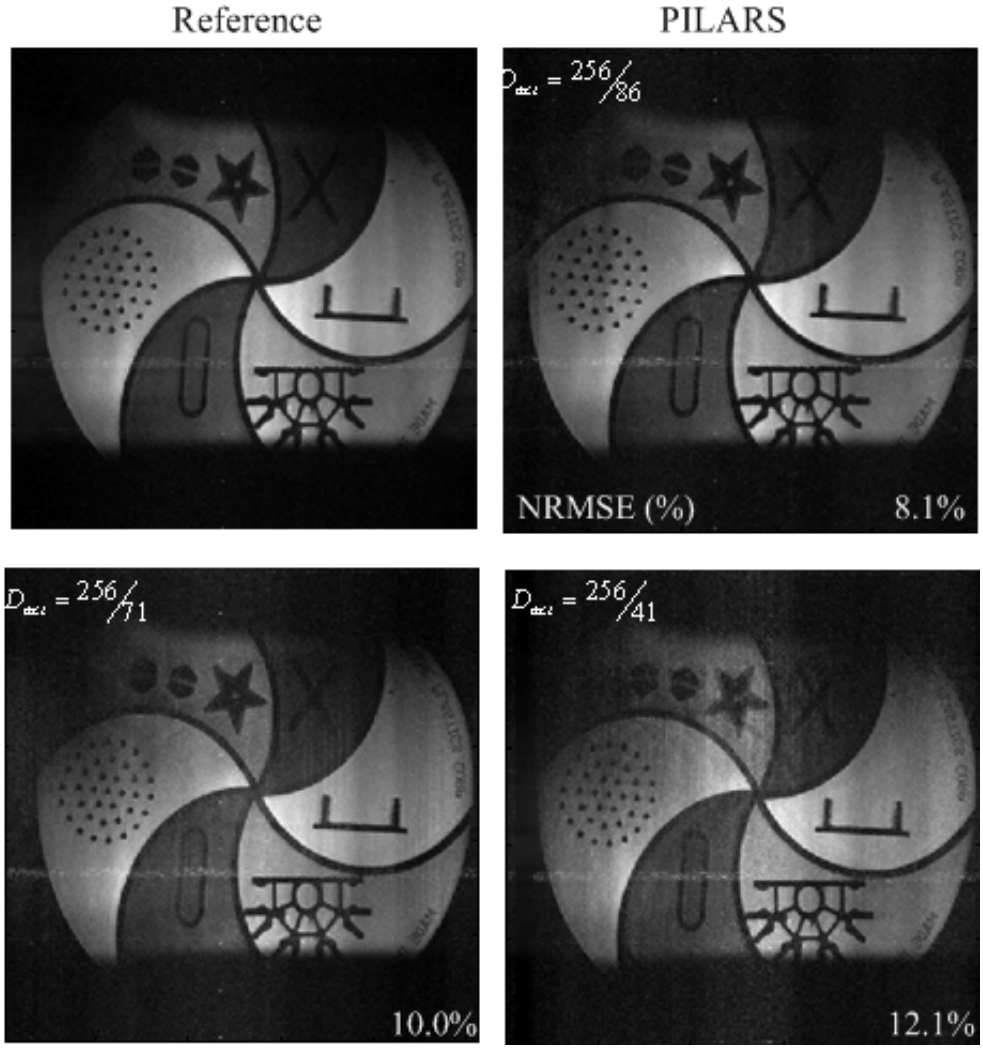

Figure 4.5: Reconstructions using the proposed PILARS method

factors.

4.5 Conclusion and Discussion

The PILS method is a well-known PI reconstruction method for highly localized arrays, which is essentially a "cut-and-paste" technique after coil centers are determined. The proposed PILARS method is different from the PILS method in several aspects. First, PILARS does not require the knowledge of the accurate location of

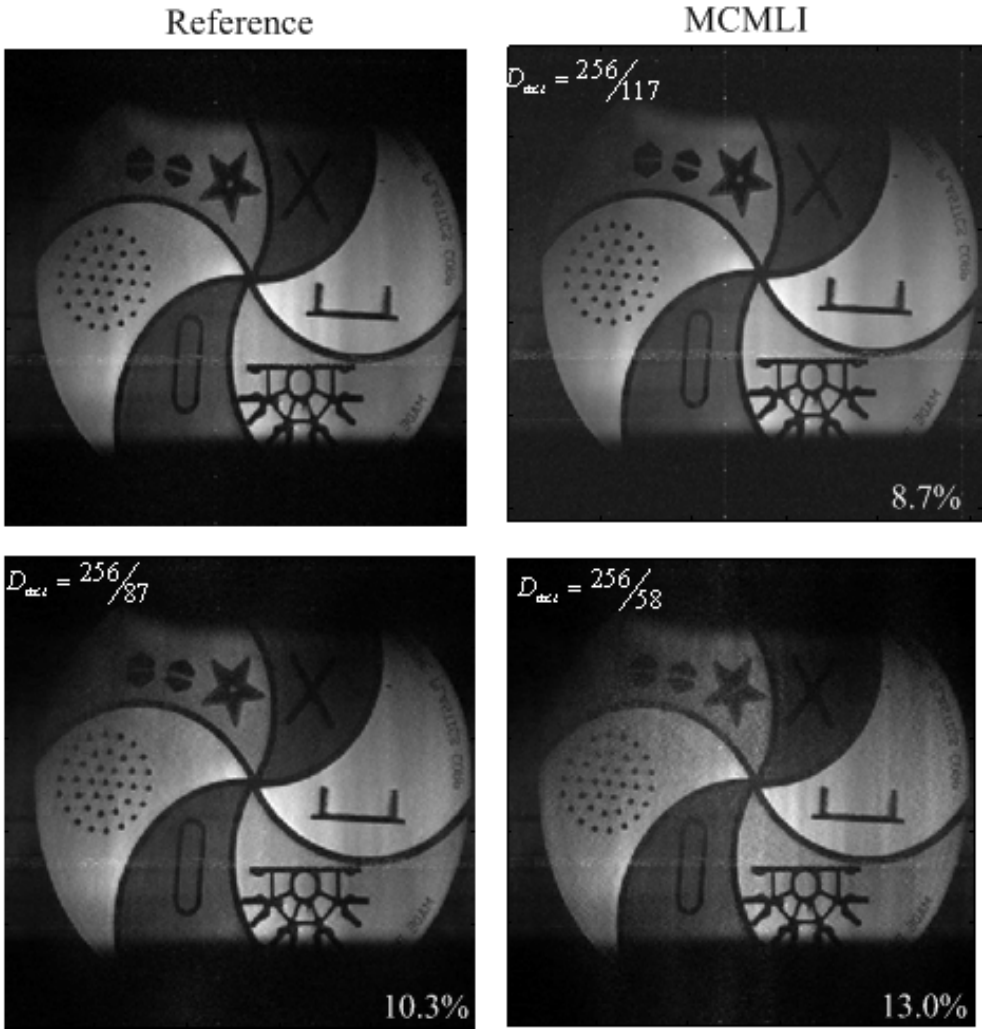

Figure 4.6: Reconstructions using the the MCMLI method

the coil element (coil sensitivity) in order to reconstruct image correctly. As shown in the simulated study, the Sinc windowing center can differ from the true coil center as it is determined by both channel sensitivity and object being imaged. Secondly, as in GRAPPA or MCMLI, PILARS can incorporate the ACS in the final reconstruction, which results in improved image quality. Finally, since the final step in the reconstruction involves sum-of-squares of all channel images and each channel has fully reconstructed data, some SNR benefit can be expected similar to GRAPPA

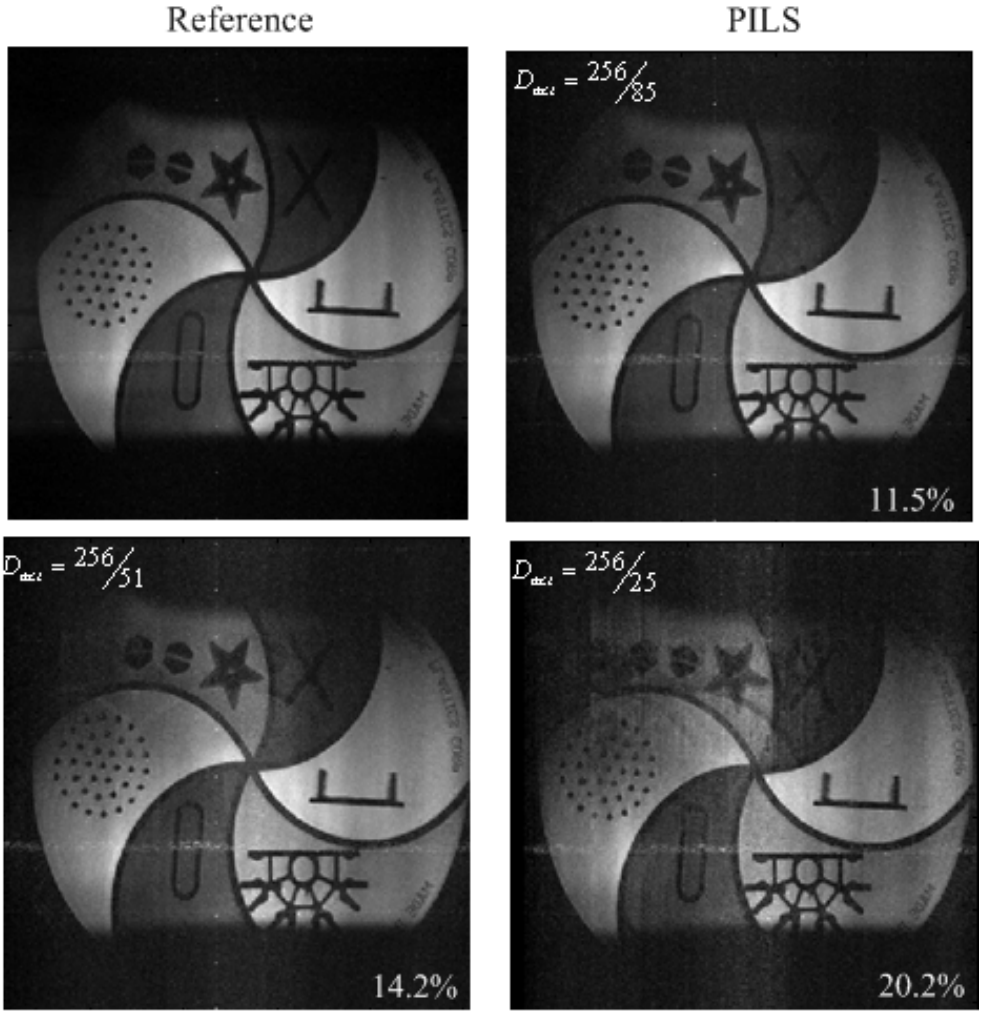

Figure 4.7: Reconstructions using the PILS method

and MCMLI.

An interesting observation of the results is that the optimal PILARS truncation window center (x_0, y_0) (in the sense of minimum error) differs from the coil sensitivity center as suggested by PILS. In both methods, the center is used to define a location of the truncation window. In PILS, it is the coil sensitivity center. In PILARS, it is estimated from acquired data, which embeds both the coil sensitivity and the underlying image object. For example, Fig. 4.3 shows that the estimated centers

Table 4.1: NRMSE verses size of ACS in the real 64-ch MRI experiment with an outer acceleration factor of $D_2 = 3$

Num. of ACS	D_{act}	NRMSE(%)	
		PILARS	MCMLI
4	2.87	7.6	19.2
8	2.74	7.3	23.4
16	2.53	6.6	10
32	2.1	5.9	8.7

Table 4.2: Reconstruction time(sec) of the three methods in the 64-ch experiment

D_2	PILARS	MCMLI	PILS
3	14	19	0.5
5	9	30	0.5
10	5	78	0.5

are shifted toward the center of the phantom image. And this leads to less power of folded artifact in the reduced FOV. As a result, PILARS yields more accurate reconstructions.

We also inspected the phase map of reconstructions. Our general observation is that when the coil image is localized, the PILARS can reconstruct phase information faithfully. Otherwise, the phase map of PILARS reconstruction is less accurate than the MCMLI, even though magnitude reconstructions are better in the sense of less NRMSE. Also, NRMSE may not be the single measurement of reconstruction quality as it only describes the total energy of artifact without error structure.

Several limitations exist for the proposed method. As in many other interpolation methods, errors can be higher at the boundary in the k-space because only partial Sinc function coefficients are available in the boundary areas. In addition, the method

is limited to arrays with highly localized elements in the imaging plane relative to the acceleration factors. A potential quantitative measure of coil locality can be defined as the ratio between the coil sensitivity energy within the reduced FOV (corresponding to the given acceleration factor) and the total coil sensitivity energy. A user-defined threshold can be applied on the ratio to determine whether the coils are localized enough for a given acceleration factor.

This paper introduced a new parallel imaging reconstruction method, which is termed as PILARS. The method is useful for parallel imaging with highly localized coil sensitivities, such as the large arrays. The reconstruction formula in the proposed method uses a Sinc kernel with predetermined interpolation coefficients and employs all acquired k-space data. A two-stage algorithm is described to determine the phase parameter needed in the interpolation. Computer simulations on both synthetic data and real MRI experiment data set showed that the new method could achieve higher actual acceleration factors with improved reconstruction quality.

5. FAST PULSE DESIGN USING GRIDDING CG

5.1 Introduction

Spatially tailored RF (TRF) pulses have contributed Magnetic Resonance Imaging (MRI) in exciting arbitrary valued spatial patterns. Parallel excitation (pTx) [26, 48, 16] techniques exploit the additional degree of freedom provided by the multiple transmit channels to shorten the RF pulse duration and reduce the specific absorption rate (SAR) [15, 6]. The combination of TRF and pTx is taken as the promising method to address challenges in the high field MRI, such as field inhomogeneity and high SAR [2].

One widely used method under the small-tip-angle approximation [33] is the spatial domain method [16]. In this method, a specified target pattern and a k-space trajectory are specified and a set of linear system equations is built. The pulses can be designed by solving the linear system using various numerical methods such as CG. One major problem of such a pulse design is the high computation cost since each iteration will require two matrix-vector multiplications. And. Generally, it can take $2-5$ minutes [41] to design a 3-D pulse, which can prevent the parallel excitation technique from being used in real-time applications. Meanwhile, the large system matrix has to be clearly specified before design which will require memory allocations on the level of several gigabyte. The entire design will require several times of that.

Currently, some methods have been reported to accelerate the spatial domain pulse design method. For example, by employing the sparsity in the excitation pattern, the design equation can be transformed into the sparse domain and truncated to reduce the computation load [11, 10]. However, the method with sparse transform can only speedup the design for up to 10 times depending on the sparsity of the tar-

get pattern. Another method [7] is reported in that the design of parallel excitation pulses can be significantly accelerated by using the CUDA enabled GPU. However, the design using GPU is limited in size due to the limit available memory on GPU (no more than 2 GB for a single GPU).

In this paper, we propose a very fast pulse design method with gridding. The two computational expensive matrix-vector multiplications are substituted by two operators, which carry out the same physical functions as the multiplications. However, the computation cost and memory cost are significantly reduced. This can be understood as the transmit version of [35]. Also, to incorporate the off-resonance term, a piece-wise linear model is adopted. By doing so, the off-resonance is incorporated into the gridding functions by shifting of the excitation trajectory and additional phase modulations. Simulation results of the proposed method shows that the design speed is improved for 8 times and the memory cost is reduced by 10^3 times with the same excitation error and convergence rate.

5.2 Theory

To solve the conventional spatial domain method, conjugate gradient method is used as described in Appendix. In each iteration of CG, the major computations (more than 90%) are consumed by two matrix-vector multiplications: $\mathbf{A}_{full}\times$ and $\mathbf{A}_{full}^H\times$. Each of these two requires $n_m n_{rf} n_c$ complex scalar multiplications, where n_m, n_{rf} and n_c are the number of pixels in the target pattern, the number of sampled points of the RF pulse for a single channel and the number of coils respectively.

5.2.1 RF Pulse Design with Gridding CG

In this section, two operators G_1 and G_2 are introduced to substitute the matrix-vector multiplications without specifying the large system matrix. The operators combine the gridding of k-space data, FFT and the sensitivity modulation. So they

are physically equivalent to the matrix-vector multiplications in the process of pulse design.

The forward operator G_1 on $b_l[t]$ will carry out the same function as the matrix-vector multiplication of the pulse of the l-th channel,

$$\mathbf{S}_l\mathbf{A}\mathbf{b}_l = G_1\{b_l[t], S_l[x], \vec{k}[t]\} \tag{5.1}$$

The $\mathbf{A}$ matrix is an inverse Fourier encoding matrix that maps $b_l[t]$ from on the non-Cartesian excitation trajectory $\vec{k}$ (e.g. spiral trajectory) to a spatial domain pattern on the Cartesian grid. Thus, it can be replaced by gridding, as in [12], followed by an inverse FFT. In the process of the gridding, the pulse (k-space data) $b_l[t]$ is first convolved with the Kaiser-Bessel kernel and then sampled on the Cartesian grid with doubled resolution corresponding to 2×FOX. The reason of sampling on a grid with finer resolution is to reduce the aliasing artifact caused by the convolution kernel in spatial domain. Then, an inverse FFT of the Cartesian data generates a spatial pattern of size 2×FOX. Then, the pattern is trimmed from the center to size of FOX and divided pixel-by-pixel by the inverse Fourier transform of the convolution kernel to compensate the convolution. After gridding, the pattern is modulated by the transmit sensitivity $S_l(x)$ and reshaped into vector form. The details of the gridding principles and procedures are given in Appendix B.

From Eq. 2.13 and Eq. 5.1, the final pattern vector is the linear sum of the pattern vectors from all channels,

$$\mathbf{m} = \sum_l \mathbf{S}_l\mathbf{A}\mathbf{b}_l = \sum_l G_1\{b_l[t], S_l[x], \vec{k}[t]\} \tag{5.2}$$

Similarly, the backward operator G_2 performed on the spatial pattern M[x] will

play the same role as the Hermitian transposed matrix-vector multiplication for the l-th channel,

$$(\mathbf{S}_l\mathbf{A})^H\,\mathbf{m} = \mathbf{A}^H\mathbf{S}_l^H = G_2\{M[x], S_l[x], \vec{k}[t]\} \tag{5.3}$$

In this backward operator, the spatial pattern is first modulated by the Hermitian transposed transmit sensitivity of the l-th channel as $\mathbf{S}_l^H\mathbf{m}$. Then, the Fourier encoding matrix $\mathbf{A}^H$, which maps the spatial domain Cartesian pattern to data on the non-Cartesian k-space trajectory $\vec{k}$, is substituted by gridding. In this gridding process, the sensitivity modulated pattern $\mathbf{S}_l^H\mathbf{m}$ is first divided pixel-by-pixel by the inverse Fourier transform of the convolution kernel and zero-padded to the size of 2×FOX. The k-space data on the Cartesian grid is then obtained by the FFT of the spatial pattern. Finally, the k-space data is convolved with the convolution kernel and sampled along the desired trajectory $\vec{k}$.

The result of the Hermitian transpose multiplication of the system matrix is a stack of vectors from individual channel results obtained from Eq. 5.3 as,

$$\begin{aligned}\mathbf{A}_{full}^H\mathbf{m} &= \left[(\mathbf{S}_1\mathbf{A})^H \cdots (\mathbf{S}_L\mathbf{A})^H\right]\mathbf{m} \\ &= \left[G_2\{M[x], S_1[x], \vec{k}[t]\} \ldots G_2\{M[x], S_L[x], \vec{k}[t]\}\right]\end{aligned} \tag{5.4}$$

The flow charts of these two matrix-vector multiplications with gridding operators are given in Fig. 5.1. Finally, the same CG method as in the conventional method will be used to solve the pulse design problem. In the steps of CG, the two multiplications are substituted by Eq. 5.2 and Eq. 5.4.

The approximate computation cost (number of complex scalar multiplications) of the operator G_1 and the direct matrix multiplication are compared in Table 5.1. Parameter $\epsilon = 2$ denotes the factor of oversampling/zero-padding and $w = 6$ is the size of convolution kernel. In the general design setup, the magnitude of n_s

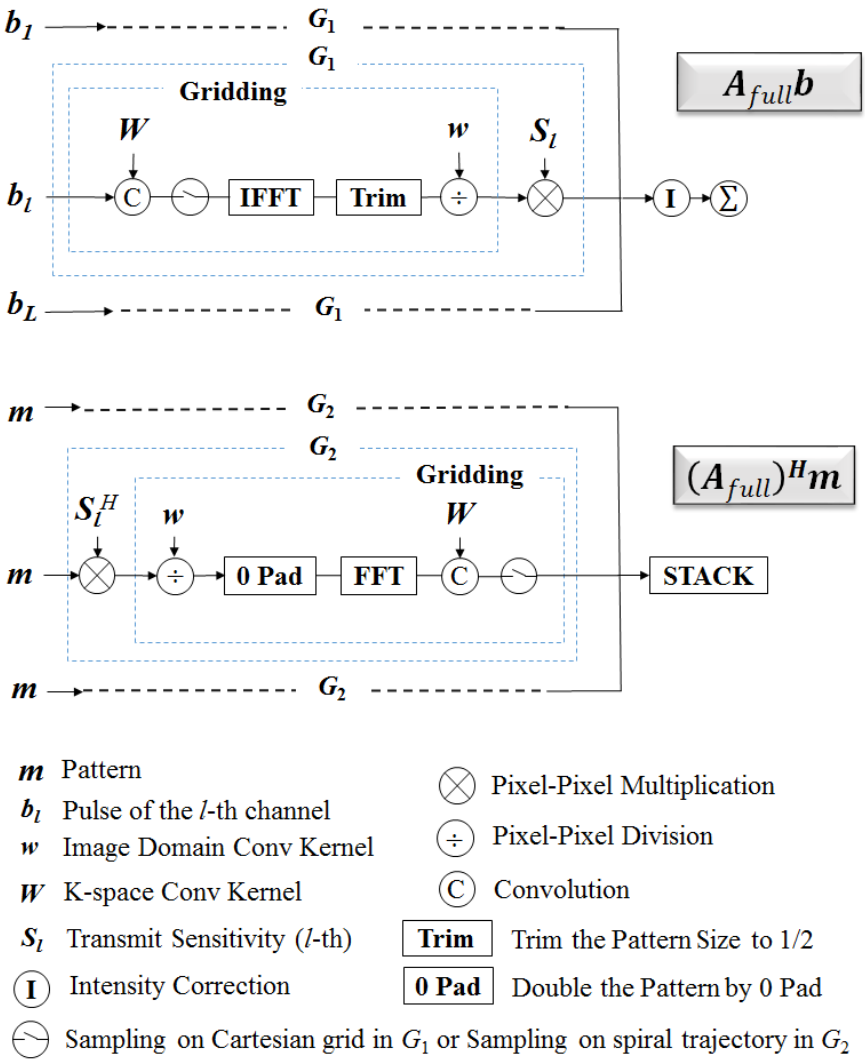

Figure 5.1: Flow chart of the two matrix-vector multiplications substituted by the two operators G_1 and G_2

and n_m are on the similar level in order to satisfy the Nyquist rate without pTx acceleration. So the computation cost is approximately reduced by the factor of $\frac{n_s}{w^2 + \epsilon^2 \log_2(\epsilon^2 n_m) + 2}$. Note that only the amount of multiplications is counted here.

For a pulse with $n_s = 1024$ to excite a target pattern defined on a grid with

$n_m = 1024$ points, the computation cost of $\mathbf{A}_{full}\mathbf{b}$ with operator G_1 for $n_c = 8$ channels is about 12 times less than the direct multiplication. As a dual pair, the computation of $\mathbf{A}_{full}^H\mathbf{m}$ with operator G_2 shares the same computation gain versus the direction corresponding matrix multiplication.

The savings in memory cost is much more significant. In the pulse design gridding CG, only several matrices of size $n_m n_c$ need to be saved. In the direction matrix multiplication, the system matrix $\mathbf{A}_{full}$ of size $n_s n_m n_c$ need to be stored. In the above example, the memory cost is reduced by about 3 magnitudes using the gridding CG method.

Table 5.1: Computation costs of $\mathbf{A}_{full}\mathbf{b}$ with operator G_1 and the direct matrix multiplication (Number of complex multiplications)

$\mathbf{A}_{full}\mathbf{b}$ with operator G_1			$\mathbf{A}_{full}\mathbf{b}$
$\otimes$	FFT	$\times$, $\div$	
$w^2 n_s n_c$	$\epsilon^2 \log_2(\epsilon^2 n_m) n_m n_c$	$2 n_m n_c$	$n_s n_m n_c$

5.2.2 Off-resonance Incorporated RF Pulse Design with Gridding CG under a Piece-wise Linear Model

Unlike the typical hard pulses, the artifact caused by main field inhomogeneity is more severe for spatial tailored pulses due to the longer pulse duration. In presence of a spatial varying off-resonance fieldmap $\Delta B_0(\vec{x})$, the gradient and off-resonance induced a net phase equals to,

$$\begin{aligned} -\gamma \int_t^T \left(\vec{x}\cdot\vec{G}(s) + \Delta B_0\right) ds \\ = \vec{x}\cdot\vec{k}(t) + \gamma \Delta B_0(\vec{x})\,(t-T) \end{aligned} \tag{5.5}$$

As proposed in [16], with knowledge of $\Delta B_0(\vec{x})$, the STA based pulse design with consideration of off-resonance is given by

$$M(\vec{x}) = i\gamma M_0 \sum_l S_l(\vec{x}) \int_0^T b_l(t) e^{i\vec{x}\vec{k}(t,T)} e^{i\gamma \Delta B_0(\vec{x})(t-T)} dt \tag{5.6}$$

In the conventional design, this additional off-resonance term only changes the value of elements in the encoding matrix $\mathbf{A}$. However, for the pulse design with gridding CG, this term cannot be easily incorporated into the gridding process since the new added term is both spatial varying and temporal varying.

To solve this problem, we can adopt a piecewise linear model [42] of $\Delta B_0(\vec{x})$, the fieldmap within each block can be expressed in linear form as

$$\Delta B_0(\vec{x}) = f_0 + \vec{f_1} \cdot \vec{x} \tag{5.7}$$

where f_0 is the baseline of the fieldmap and $\vec{f_1}$ is a constant vector with the same dimension as $\vec{k}$ which describes the direction of the linear off-resonance map. By plugging Eq. 5.7 into Eq. 5.6, we get a STA Bloch equation with the off-resonance term incorporated into other existing terms,

$$M(\vec{x}) = i\gamma M_0 \sum_l S'_l(\vec{x}) \int_0^T b'_l(t) e^{i\vec{x}\vec{k}_{shift}(t,T)} dt \tag{5.8}$$

where $s'_l(\vec{x}) = s_l(\vec{x}) e^{i\phi_1(\vec{x})}$, $b'_l = b_l(t) e^{i\phi_2(t)}$, $\phi_1(\vec{x}) = -\gamma \Delta B_0(\vec{x}) T$, $\phi_2(t) = \gamma f_0 t$ and $\vec{k}_{shift}(t) = \vec{k}(t,T) + \gamma t \vec{f_1}$.

This indicates that to incorporate the off-resonance term into the proposed gridding CG method, three terms need to be modified. The first term is a spatial domain phase modulation $e^{i\phi_1}$ which contains the original fieldmap without approximation. It is modulated to the spatial transmit sensitivity $s_l(\vec{x})$. The second term is a time

domain phase modulation $e^{i\phi_2}$ which is induced by the 0^{th} order component of the fieldmap $\Delta B_0(\vec{x})$. It is modulated to the pulse $b_l(t)$. The last modification is caused by the 1^{st} order component of the fieldmap. It is equivalent to encoding gradient and leads to a time-varying shift of the original excitation trajectory by $\gamma t\vec{f_1}$. The end of the excitation trajectory is shifted most by the amount of $\gamma T\vec{f_1}$ from the origin. All of these three modifications are universally applied to all channels in both the operator G_1 and G_2.

Assume that the entire FOX can be partitioned into multiple blocks and this linear off-resonance model as described by Eq. 5.7 stands well within all blocks. Let the off-resonance map of the q-th block be $\Delta B_0^q(\vec{x}) = f_0^q + \vec{f_1^q} \cdot \vec{x}$ for $\vec{x} \in q$, we can have a discrete version of Eq. 5.8 for this block with three modified terms as,

$$\mathbf{m}^q = \sum_l \mathbf{S}_l^q \mathbf{A}^q \mathbf{b}_l^q \tag{5.9}$$

where $\mathbf{S}_l^q$ is the modulated sensitivity for the q-th block of the l-th chanel, $\mathbf{A}^q$ is the Fourier encoding matrix defined on the shifted trajectory for the q-th block and $\mathbf{b}_l^q$ is the phase modulated pulse for the q-the block of the l-th channel. $\mathbf{m}^q$ is set to zero for locations outside the q-th block.

By employing the two operators G_1 and G_2, the matrix-vector multiplications can be substituted by the operators similar to Eq. 5.2 and Eq. 5.4 as

$$\mathbf{m}^q = \sum_l \mathbf{S}_l^q \mathbf{A}^q \mathbf{b}_l^q = \sum_l G_1\{b_l^q[t], S_l^q[x], \vec{k}_{shift}^q[t]\} \tag{5.10}$$

and the final pattern is a combination of the pattern from all blocks

$$\mathbf{m} = \mathbf{A}_{full}\mathbf{b} = \sum_q \mathbf{m}^q \tag{5.11}$$

Similarly, the substitute of the Hermitian transposed matrix-vector multiplication with gridding for the q-th block is given by

$$\begin{aligned}\mathbf{A}_{full}^{H}\mathbf{m}^{q} &= \left[\left(\mathbf{S}_{1}^{q}\mathbf{A}^{q}\right)^{H}\cdots\left(\mathbf{S}_{L}^{q}\mathbf{A}^{q}\right)^{H}\right]\mathbf{m}^{q} \\ &= \left[G_{2}\{M^{q}[x],S_{1}^{q}[x],\vec{k}_{shift}^{q}[t]\}\ldots G_{2}\{M^{q}[x],S_{L}^{q}[x],\vec{k}_{shift}^{q}[t]\}\right]\end{aligned} \tag{5.12}$$

where $M^{q}[x]=M[x]$ for $x\in q$ and 0 elsewhere is the q-th block of the partitioned pattern, S_{l}^{q} is the modified transmit sensitivity for the l-th channel and the q-th block and $\vec{k}_{shift}^{q}$ is the shifted excitation trajectory for the q-the block. The final Hermitian transposed matrix-vector multiplication is the sum of results from all blocks,

$$\mathbf{A}_{full}^{H}\mathbf{m}=\sum_{q}\mathbf{A}_{full}^{H}\mathbf{m}^{q} \tag{5.13}$$

With these modified operator substitutes, the proposed pulse design method with gridding CG is able to incorporate the off-resonance under a piecewise linear model. Three terms need to be modified for each block according to the linear coefficient of the off-resonance map. The phase modulation on the transmit sensitivities are universal for all channels and all CG iterations and is done for only once. The shift of the k-space trajectory need to be done once for each block. But the second phase modulation on pulse is performed twice in each iteration and for each block. Thus, the computation cost of pulse design with gridding CG is linearly proportional to the number of blocks in presence of off-resonance.

5.3 Methods

5.3.1 2D Pulse Design with Gridding CG

To evaluate the performance of the proposed design method, a 2-D tailored pulse will be designed to excite a 2-D pattern as in Fig. 5.2(a) over a $20\times 20\text{cm}^2$ FOX.

An 8-ch linear transmit array and a spiral trajectory as in Fig. 5.2(b) with 2× pTx acceleration are used for the design using the proposed method and the conventional spatial domain method. The total pulse length is 5.3$m$sec with a dwell time of 0.0026$m$sec.

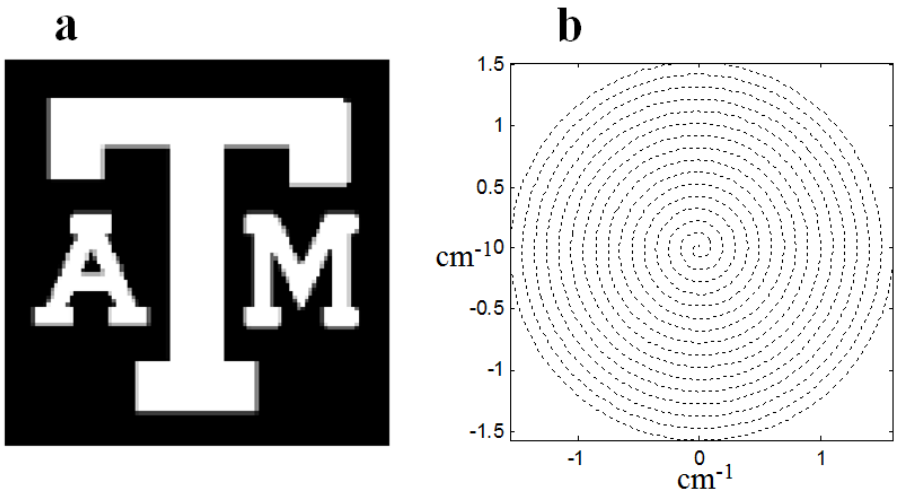

Figure 5.2: (a) The target pattern for the pulse design and (b) the excitation k-space trajectory with acceleration of $R = 2$

It is assumed that there is no off-resonance effect in this experiment. And both methods are performed with exactly the same setup, including parameters, transmit sensitivities and the target pattern. The residual of each CG iteration is measured by the l_2 norm of the current residual vector which can show the convergence. And the quantitative difference between the two methods in term of designed pulse, excitation error, design time and memory cost are compared. The excitation patterns for excitation error measurement are obtained from the Bloch simulator.

The gridding part in operator G_1 is implemented using an online NUFFT toolbox. And the gridding part in operator G_2 is implemented with the'interp2' function

provided by the interpolation toolbox in Matlab. Proper modifications including phase correction, zero-padding and intensity correction are made.

5.3.2 Pulse Design in Presence of Off-resonance

To evaluate the proposed method in presence of off-resonance, a 2D pulse design experiment with a simple off-resonance map is performed. The off-resonance map is partitioned into three linear blocks. The linear off-resonance coefficients in each block are f_0 = -70 Hz, 30 Hz and 20 Hz and $\vec{f_1} = [-15, 5]^T$ Hz/cm, $[-10, 0]^T$ Hz/cm and $[15, -5]^T$ Hz/cm respectively. All the other parameters including the target pattern and excitation trajectory follow the setup from the previous experiment. This off-resonance map is shown in Fig. 5.3.

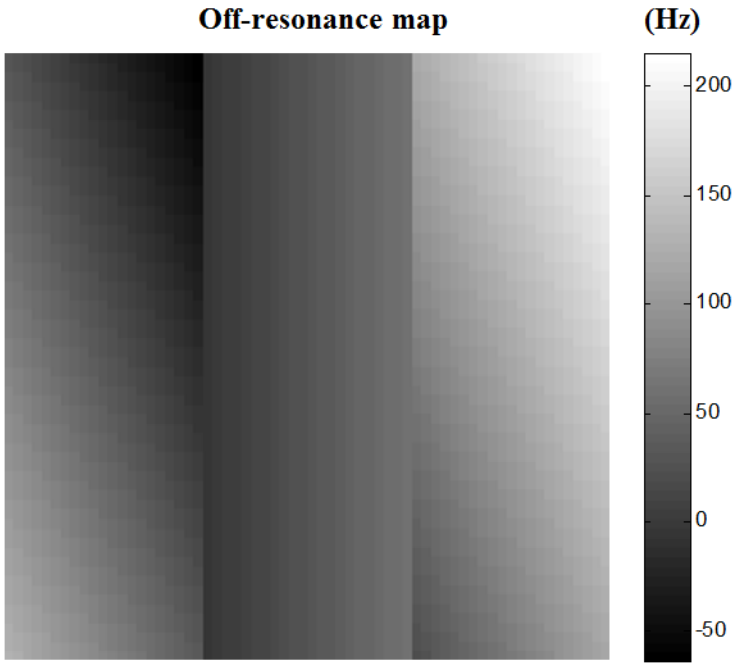

Figure 5.3: The off-resonance map that contains three different blocks, linear within each block, the range of ΔB_0 over the entire FOX is 280Hz

The proposed pulse design method with gridding CG is used to design pTx pulses with the off-resonance information incorporated. The conventional spatial domain method is also used to design pulses for comparison. The time cost of the pulse designs are recorded and the final excitation patterns of the designed pulses are evaluated using the Bloch simulator.

5.3.3 Design Stability to Inaccurate B_1^+ Maps

In this simulation, the stability to inaccurateB_1^+ sensitivities of the proposed method is tested and compared with the conventional method. Complex Gaussian noise is added to the trueB_1^+ sensitivities. The SNR of the B_1^+ sensitivity is defined as SNR $= 10\log_{10}\left(\frac{P_s}{P_n}\right)$, where P_s is the average power of true B_1^+ sensitivity of all the channels and P_n is the power of the added Gaussian noise.

The pulses are designed with the noise corrupted B_1^+ sensitivities with different SNR using the conventional method and the proposed method. A pTx acceleration of 2 is used in all designs. The spiral-in trajectory and transmit sensitivity are the same as that in previous experiments. The excitation patterns are obtained using the Bloch simulator with the true B_1^+ sensitivity without noise. In this experiment, it is assumed that there is no off-resonance effect.

All simulations are performed in Matlab 2011b (Math Works, Natick, MA) on a desktop with 2.67GHz i-7 CPU and 9 GB memory.

5.4 Results

The pulse design result of the experiment on designing 2D ptx in the absence of off-resonance is given in Fig. 5.4. The residual curve of the proposed method is shown in Fig. 5.4(a). And its relative difference in residuals comparing to the conventional design is shown in Fig. 5.4(b). As can be seen, the CG in the proposed method converges towards zero at the same rate as the conventional method and the

relative difference is within 0.5%. The excitation patterns from the Bloch simulator are shown in Fig. 5.4(c). Both the methods lead to an normalized root mean square error of 5.65% as expected, because the maximum error of a single gridding step is controlled below 0.1%. Thus, the proposed method can achieve the same accuracy as the conventional method.

The time consumed by the matrix-vector multiplication with operator G_1 and the direct multiplication in the conventional design are 2.3 sec and 18 sec respectively in 100 times of iteration. Similar gain is observed for the Hermitian transposed matrix-vector multiplication with G_2. And the total design time is reduced by about 10 fold using the proposed method.

The system matrix $\mathbf{A}_{full}$ alone requires 1012 MB memory in the conventional method. In the pulse design with gridding CG, it requires no more than 5 MB memory in total. Thus, the memory cost of the proposed method is improved by about 3 magnitudes.

The excitation patterns of the proposed method are shown in Fig. 5.6. The excitation error of the magnitude pattern is 9.5% comparing to the 9.4% in the conventional method as in Fig. 5.5. The phase error pattern of both methods as in Fig. 5.5(b) and Fig. 5.6(b). They are both zero in the excited region in FOX. Thus the off-resonance effect has been correctly countered during the excitation using both methods.

The excitation errors are very close. However, the design time of the proposed method is 16.5 sec comparing to the 41.3 sec of the conventional method. Note that the computation gain has been reduced by about 3 times which is due to the 2 additional blocks. The benefit of memory saving using the proposed method is still about the magnitude of 3 in this case.

Excitation errors of the pulses designed using the conventional method and the

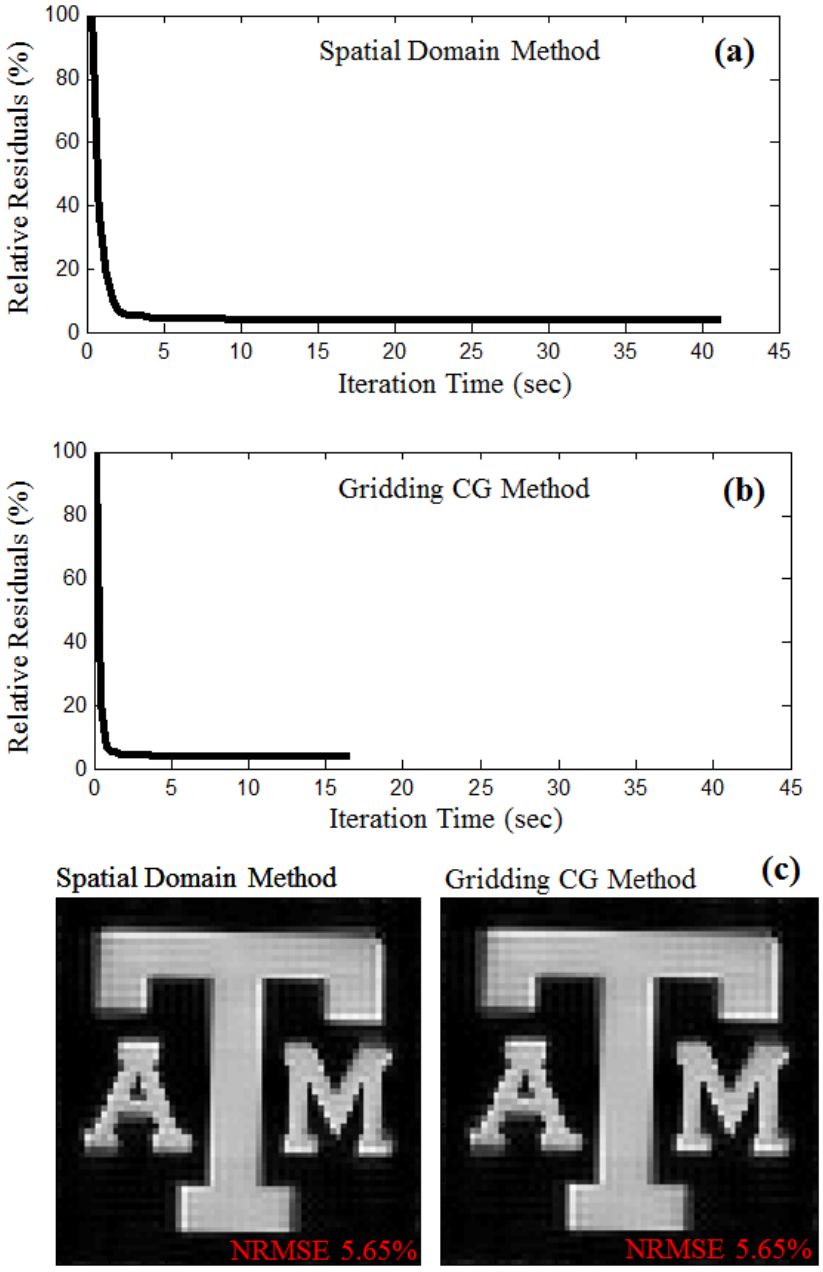

Figure 5.4: Relative residuals (a) of the pulse design using the spatial domain method versus design time and the relative residuals (b) of the pulse design using the gridding CG method. 100 iterations are performed for both. (c) The excitation patterns of the two methods

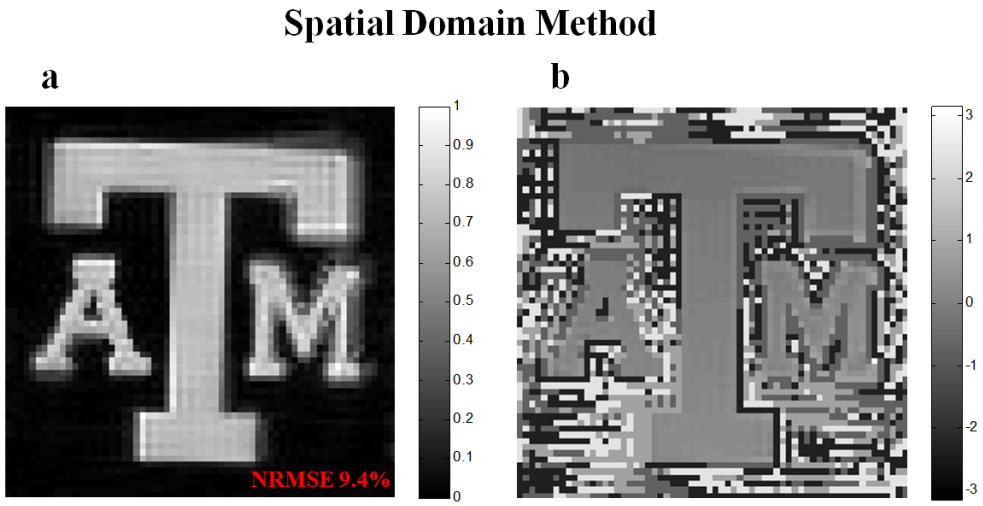

Figure 5.5: The excitation patterns of pulse designed using the conventional design method: (a) the magnitude pattern and (b) the phase error pattern in presence of off-resonance

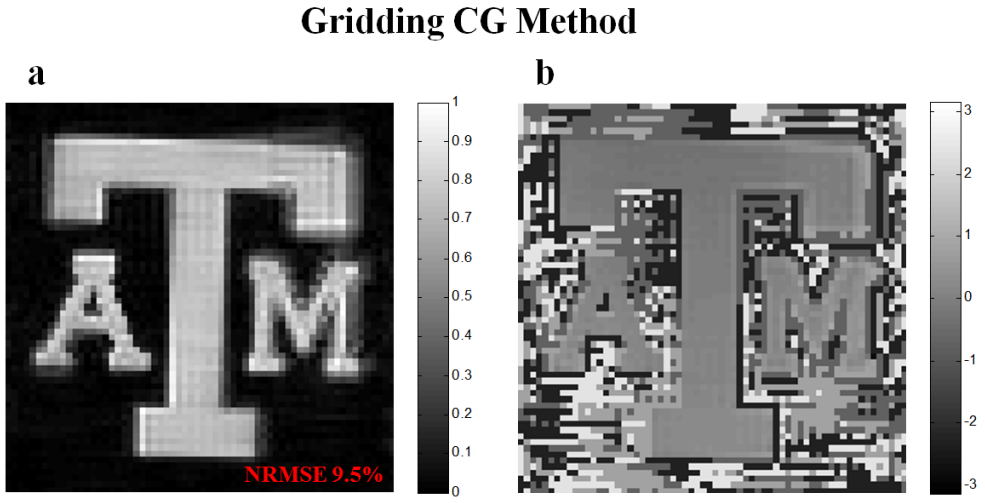

Figure 5.6: The excitation patterns of pulse designed using the proposed design method: (a) the magnitude pattern and (b) the phase pattern in presence of off-resonance

proposed method are shown in Fig. 5.7. As the SNR of the B_1^+ sensitivities increases, the error decreases for both the methods. The error curves of these two methods are almost the same. Thus, the proposed method has the same stability to inaccurate B_1^+ measurement as the conventional method. But the design speed of the proposed method is 10 times faster than the conventional method on average.

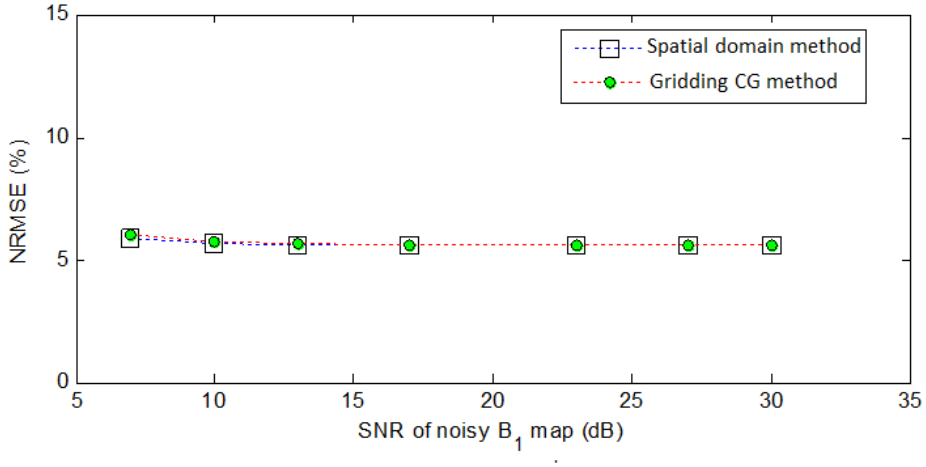

Figure 5.7: Excitation error versus the SNR of the B_1+ sensitivities

5.5 Conclusion

In this work, we proposed a very fast pulse design method based on the spatial domain method with gridding CG. The matrix-vector multiplications, which are computational expensive in the conventional method, are substituted by two operators which include data gridding, sensitivity modulation and multiple channel combinations. The design speed can be improved by about 10 times theoretically and validated in the experiment. To incorporate off-resonance into the proposed method, a piecewise linear model is adopted. FOX is partitioned into blocks with linear off-resonance. Then, three terms are modified to incorporate the off-resonance

information into the pulse design gridding CG. Simulation results show that the proposed pulse can achieve the same design accuracy as the conventional method in both absence and presence of off-resonance. The computation cost of the proposed method increases linearly with the number of blocks.

The memory cost can be reduced by 10^3 times by using the proposed method. This eases the memory burden of designing longer pTx pulses with more transmit channels or exciting a pattern defined on a grid with finer resolution. Meanwhile, the memory bottleneck of implementing the pulse designs on GPU is completely broken. The proposed operators are implemented on a channel by channel base and can be easily paralleled. All these promise a further speedup of 20 times of the proposed method.

5.6 Discussion

To the best knowledge of author, this pulse design method using gridding CG can be used to accelerate the pulse designs in any existing pulse design methods based on the spatial domain method. Pulse design with regularization terms such as to control the average SAR or maximum SAR can be simply added to the pulse design with gridding CG with little change of total computation costs.

In the experiment of pulse design in presence of off-resonance, 3 linear off-resonance blocks were manually setup. This should be replaced by some partition algorithms to minimize the model error in practical implementation which will be included in our future work.

6. SUMMARY

This dissertation focuses on the parallel imaging and parallel excitation techniques in MRI. Three major contributions are made. All these proposed work are designed for large arrays with a large number of elements.

First, a correlation based channel reduction algorithm is developed to reduce the computation cost of PI reconstructions. With the same level of reconstruction quality, the reconstruction speed is enhanced. Second, a new parallel imaging method named PILARS is proposed to either improve the actual acceleration factor for shorter imaging time or and reduce the computation cost with the similar or improved reconstruction quality comparing to existing methods.Finally, a fast pTx pulse design method is proposed to accelerate the pulse design speed in pTx. These contributions can tremendously improve the efficiency of PI and pTx using large arrays.

REFERENCES

[1] Gregor Adriany, Edward J Auerbach, Carl J Snyder, Ark Gözübüyük, Steen Moeller, Johannes Ritter, Van de Moortele, Tommy Vaughan, Kamil Uğurbil, et al. A 32-channel lattice transmission line array for parallel transmit and receive MRI at 7 Tesla. *Magnetic Resonance in Medicine*, 63(6):1478–1485, 2010.

[2] Peter A Bandettini, Richard Bowtell, Peter Jezzard, and Robert Turner. Ultra-high field systems and applications at 7 T and beyond: progress, pitfalls, and potential. *Magnetic Resonance in Medicine*, 67(2):317–321, 2012.

[3] JC Bosshard and SM Wright. High speed MR elastography using SEA imaging. In *Proceedings of the 16th Annual Meeting of ISMRM*, Toronto, Ontario, Canada, 2008.

[4] AC Brau, PJ Beatty, S Skare, and R Bammer. Comparison of reconstruction accuracy and efficiency among autocalibrating data-driven parallel imaging methods. *Magnetic Resonance in Medicine*, 59:382–395, 2008.

[5] Martin Buehrer, Klaas P Pruessmann, Peter Boesiger, and Sebastian Kozerke. Array compression for MRI with large coil arrays. *Magnetic Resonance in Medicine*, 57(6):1131–1139, 2007.

[6] Christopher M Collins, Shizhe Li, and Michael B Smith. SAR and B1 field distributions in a heterogeneous human head model within a birdcage coil. *Magnetic Resonance in Medicine*, 40(6):847–856, 2005.

[7] Weiran Deng, Cungeng Yang, and V Andrew Stenger. Accelerated multidimensional radiofrequency pulse design for parallel transmission using concurrent computation on multiple graphics processing units. *Magnetic Resonance in Medicine*, 65(2):363–369, 2011.

[8] Mariya Doneva and Peter Börnert. Automatic coil selection for channel reduction in SENSE-based parallel imaging. *Magnetic Resonance Materials in Physics, Biology and Medicine*, 21(3):187–196, 2008.

[9] Shuo Feng and Jim Ji. Channel reduction in massive array parallel MRI. In *31st Annual International Conference of the IEEE EMBS*, pages 4045–4048, Hawaii, USA, September 2-6 2009.

[10] Shuo Feng and Jim Ji. A novel fast algorithm for parallel excitation pulse design in MRI. In *Engineering in Medicine and Biology Society (EMBC), 2012 Annual International Conference of the IEEE*, pages 1102–1105, San Diego, California, USA, 2012.

[11] Shuo Feng and Jim Ji. An Algorithm for Fast Parallel Excitation Pulse Design. In *Proceedings of the 21th Annual Meeting of ISMRM*, Salt Lake City, Utah, USA, 2013.

[12] Shuo Feng and Jim X. Ji. PILARS: parallel imaging with large arrays and Sinc-interpolation. In *In: Proceedings of the 19th Annual Meeting of ISMRM.*, page 4652, Montreal, Quebec, Canada, 2011.

[13] Shuo Feng, Yudong Zhu, and Jim Ji. Efficient large-array k-domain parallel MRI using channel-by-channel array reduction. *Magnetic Resonance Imaging*, 29(2):209–215, 2011.

[14] Rafael C Gonzalez, Richard E Woods, and Steven L Eddins. *Digital Image Processing Using MATLAB*, volume 2. Gatesmark Publishing Knoxville, 2009.

[15] Ingmar Graesslin, Hanno Homann, Sven Biederer, Peter Börnert, Kay Nehrke, Peter Vernickel, Giel Mens, Paul Harvey, and Ulrich Katscher. A specific absorption rate prediction concept for parallel transmission MR. *Magnetic Resonance in Medicine*, 68(5):1664–1674, 2012.

[16] William Grissom, Chun-yu Yip, Zhenghui Zhang, V Andrew Stenger, Jeffrey A Fessler, and Douglas C Noll. Spatial domain method for the design of RF pulses in multicoil parallel excitation. *Magnetic Resonance in Medicine*, 56(3):620–629, 2006.

[17] MA Griswold, PM Jakob, RM Heidemann, M Nittka, V Jellus, J Wang, B Kiefer, and A Haase. Generalized autocalibrating partially parallel acquisitions (GRAPPA). *Magnetic Resonance in Medicine*, 47(6):1202–1210, 2002.

[18] Mark A Griswold, Peter M Jakob, Mathias Nittka, James W Goldfarb, and Axel Haase. Partially parallel imaging with localized sensitivities (PILS). *Magnetic Resonance in Medicine*, 44(4):602–609, 2000.

[19] Christopher J. Hardy, Randy O. Giaquinto, Joseph E. Piel, Kenneth W. Rohling AAS, Luca Marinelli, Daniel J. Blezek, Eric W. Fiveland, Robert D. Darrow, and Thomas K.F. Foo. 128-channel body mri with a flexible high-density receiver-coil array. *Journal of Magnetic Resonance Imaging*, 28(5):1219–1225, 2008.

[20] K Heberlein. Automated coil subset selection for improved GRAPPA reconstruction. In *In: Proceedings of the 17th Annual Meeting of ISMRM.*, volume 17, page 761, Hawaii, USA, 2009.

[21] Robin M Heidemann, Mark A Griswold, Axel Haase, and Peter M Jakob. VD-AUTO-SMASH imaging. *Magnetic Resonance in Medicine*, 45(6):1066–1074, 2001.

[22] Feng Huang, Sathya Vijayakumar, Yu Li, Sarah Hertel, and George R Duensing. A software channel compression technique for faster reconstruction with many channels. *Magnetic Resonance Imaging*, 26(1):133–141, 2008.

[23] John I Jackson, Craig H Meyer, Dwight G Nishimura, and Albert Macovski. Selection of a convolution function for Fourier inversion using gridding. *IEEE Transactions on Medical Imaging*, 10(3):473–478, 1991.

[24] Peter M Jakob, Mark A Grisowld, Robert R Edelman, and Daniel K Sodickson. AUTO-SMASH: a self-calibrating technique for SMASH imaging. *Magnetic Resonance Materials in Physics, Biology and Medicine*, 7(1):42–54, 1998.

[25] Jim X Ji, Jong Bum Son, and Swati D Rane. PULSAR: A Matlab toolbox for parallel magnetic resonance imaging using array coils and multiple channel receivers. *Concepts in Magnetic Resonance Part B: Magnetic Resonance Engineering*, 31(1):24–36, 2007.

[26] Ulrich Katscher, Peter Börnert, Christoph Leussler, and Johan S van den Brink. Transmit SENSE. *Magnetic Resonance in Medicine*, 49(1):144–150, 2002.

[27] Walid E Kyriakos, Lawrence P Panych, Daniel F Kacher, Carl-Fredrick Westin, Sumi M Bao, Robert V Mulkern, and Ferenc A Jolesz. Sensitivity profiles from an array of coils for encoding and reconstruction in parallel (SPACE RIP). *Magnetic Resonance in Medicine*, 44(2):301–308, 2000.

[28] RF Lee, H Chang, C Stefanescu, B Stoeckel, D Santoro, D Strick, R Xue, N Oessingman, G Johnson, and D Sodickson. A 128-channel helium-3 phased array at 3T for highly accelerated parallel imaging in hyperpolarized gas MRI. In *Proceedings of the 16th Annual Meeting of ISMRM.*, Toronto, Ontario, Canada, 2008.

[29] M Lustig and JM Pauly. SPIRiT: Iterative self consistent parallel imaging reconstruction from arbitrary k space. *Magnetic Resonance in Medicine*, 64(2):457–471, 2010.

[30] Weihua Mao, Michael B Smith, and Christopher M Collins. Exploring the limits of RF shimming for high-field MRI of the human head. *Magnetic Resonance in Medicine*, 56(4):918–922, 2006.

[31] Mary Preston McDougall and Steven M Wright. 64-channel array coil for single echo acquisition magnetic resonance imaging. *Magnetic Resonance in Medicine*, 54(2):386–392, 2005.

[32] John Pauly, Patrick Le Roux, Dwight Nishimura, and Albert Macovski. Parameter relations for the Shinnar-Le Roux selective excitation pulse design algorithm. *IEEE Transactions on Medical Imaging*, 10(1):53–65, 1991.

[33] John Pauly, Dwight Nishimura, and Albert Macovski. A k-space analysis of small-tip-angle excitation. *Journal of Magnetic Resonance*, 81(1):43–56, 1989.

[34] John G Proakis, F Ling, and C Nikias. *Advanced Topics in Digital Signal Processing*. Prentice Hall Professional Technical Reference, 1992.

[35] Klaas P Pruessmann, Markus Weiger, Peter Börnert, and Peter Boesiger. Advances in sensitivity encoding with arbitrary k-space trajectories. *Magnetic Resonance in Medicine*, 46(4):638–651, 2001.

[36] Klaas P Pruessmann, Markus Weiger, Markus B Scheidegger, Peter Boesiger, et al. SENSE: sensitivity encoding for fast MRI. *Magnetic Resonance in Medicine*, 42(5):952–962, 1999.

[37] Peng Qu, Gary X Shen, Chunsheng Wang, Bing Wu, and Jing Yuan. Tailored utilization of acquired k-space points for GRAPPA reconstruction. *Journal of Magnetic Resonance*, 174(1):60–67, 2005.

[38] Volker Rasche, Roland Proksa, R Sinkus, Peter Bornert, and Holger Eggers. Resampling of data between arbitrary grids using convolution interpolation. *IEEE Transactions on Medical Imaging*, 18(5):385–392, 1999.

[39] PB Roemer, WA Edelstein, CE Hayes, SP Souza, and OM Mueller. The NMR phased array. *Magnetic Resonance in Medicine*, 16(2):192–225, 1990.

[40] Alexey A Samsonov. On optimality of parallel MRI reconstruction in k-space. *Magnetic Resonance in Medicine*, 59(1):156–164, 2007.

[41] Kawin Setsompop, Lawrence L Wald, Vijayanand Alagappan, Borjan Gagoski, Franz Hebrank, Ulrich Fontius, Franz Schmitt, and Elfar Adalsteinsson. Parallel RF transmission with eight channels at 3 Tesla. *Magnetic Resonance in Medicine*, 56(5):1163–1171, 2006.

[42] Travis B Smith and Krishna S Nayak. Automatic off-resonance correction in spiral imaging with piecewise linear autofocus. *Magnetic Resonance in Medicine*, 69(1):82–90, 2013.

[43] Daniel K Sodickson and Warren J Manning. Simultaneous acquisition of spatial harmonics (SMASH): fast imaging with radiofrequency coil arrays. *Magnetic Resonance in Medicine*, 38(4):591–603, 2005.

[44] Jong Bum Son, Jim X Ji, Mary P McDougall, and Steve M Wright. Adaptive SENSE reconstruction for parallel imaging with massive array coils. In *Engineering in Medicine and Biology Society, 2004. IEMBS'04. 26th Annual International Conference of the IEEE*, volume 1, pages 1064–1067, San Francisco, California, USA, 2004.

[45] JL Ulloa, P Irarrazaval, and JV Hajnal. Exploring 3D RF shimming for slice selective imaging. In *Proceedings of the 13th Annual Meeting of ISMRM*, page 21, Miami Beach, FL, USA, 2005.

[46] Ze Wang, Jiongjiong Wang, and John A Detre. Improved data reconstruction method for GRAPPA. *Magnetic Resonance in Medicine*, 54(3):738–742, 2005.

[47] SM Wright. Multidisciplinary approaches to MR engineering. In *Proceedings of the Joint Annual Meeting ISMRM-ESMRMB*, Hamburg, Germany, 2007.

[48] Yudong Zhu. Parallel excitation with an array of transmit coils. *Magnetic Resonance in Medicine*, 51(4):775–784, 2004.

APPENDIX A

CONJUGATE GRADIENT SOLVER

The conjugate gradient method that has been using the to solve the pulse design problem is explain below.

$$
\begin{aligned}
\text{Initial:} \quad & z_0 = m \\
& r_0 = \mathbf{A}^T z_0 \\
& p_0 = r_0 \\
& x_0 = 0 \\
& \phi_0 = ||r_0||^2 \\
\text{Iterate:} j \quad & c_{j-1} = \mathbf{A} p_{j-1} \\
& p_0 = r_0 \\
& \alpha_{j-1} = \frac{\phi_{j-1}}{||c_{j-1}^2|| + \lambda ||p_{j-1}||^2} \\
& x_j = x_{j-1} + \alpha_{j-1} p_{j-1} \\
& z_j = z_{j-1} - \alpha_{j-1} p_{j-1} \\
& r_j = \mathbf{A}^T - \lambda x_j \\
& \phi_j = ||r_j||^2 \\
& \beta_{j-1} = \frac{\phi_j}{\phi_{j-1}} \\
& p_j = r_j + \beta_{j-1} p_{j-1}
\end{aligned}
$$

The computation cost hotspot is two matrix-vector multiplications within the iteration. All the other multiplications are scalar-vector, scalor-vector or vector inner product multiplications which are computationally neglectable comparing to the hotspot.

APPENDIX B

GRIDDING: RECONSTRUCTION OF NON-CARTESIAN K-SPACE DATA

The gridding process maps the non-Cartesian k-space pulse $b(t)$ to a Cartesian pattern in spatial domain $m(\vec{x})$. It employs the fast Fourier transform to reduced the computation cost of the Fourier encoding and can be understood as a data re-sampling process after convolution interpolation [38]. In this section, we start with the general formula that all functions are defined continuously. The spatial domain functions are denoted in lower case and the k-space functions in capital case.

Let $B(\vec{k})$ be the signal in k-space which is the continuous RF pulse in our case. Let $O_{Spr}(\vec{k})$ be the sampling function on arbitrary trajectory such as the spiral trajectory and $O_{Cart}(\vec{k})$ be the sampling function on the Cartesian grid. Thus, the goal is to calculate the spaital pattern

$$m = \mathcal{F}\mathcal{T}^{-1}\left(B \cdot O_{Spr}\right) \tag{B.1}$$

from acquired non-Cartesion data $B \cdot O_{Spr}$.

In order to take advantage of the computation speed of the Fast Fourier transform, we need map the non-Cartesian k-space data onto Cartesion grid first. And this goal is achieved by convolution interpolation.

Let $C(\vec{k})$ be a convolution function and $c(\vec{x})$ is its Fourier pair. A continuous k-space function is obtained by convolving the data we have $B \cdot O_{Spr}$ with the convolution function C as

$$\left(B \cdot O_{Spr}\right) \otimes C \tag{B.2}$$

Then, the Cartesian k-space data is obtained by sampling with O_{Cart} as,

$$(B \cdot O_{Spr}) \otimes C \cdot O_{Cart} \tag{B.3}$$

of which the corresponding spatial pattern can be calculated as,

$$\begin{aligned} &\mathcal{FFT}^{-1}\left[(B \cdot O_{Spr}) \otimes C \cdot O_{Cart}\right] \\ =&\mathcal{FT}^{-1}\left(B \cdot O_{Spr}\right) \cdot c \otimes \mathcal{FT}^{-1}(O_{Cart}) \\ =&\mathcal{FT}^{-1}\left(B \cdot O_{Spr}\right) \cdot c \end{aligned} \tag{B.4}$$

Here both the operator $\mathcal{FT}$ and $\mathcal{FFT}$ represents the same Fourier transform but the second one is implemented using the fast Fourier transform. The inverse Fourier transform of the Cartesian sampling function $\mathcal{FT}^{-1}(O_{Cart})$ equals to one and omitted with proper sampling rate.

Thus, we have the reconstructed spatial domain pattern,

$$\begin{aligned} m &= \mathcal{FT}^{-1}\left(B \cdot O_{Spr}\right) \\ &= \frac{\mathcal{FFT}^{-1}\left[(B \cdot O_{Spr}) \otimes C \cdot O_{Cart}\right]}{c} \end{aligned} \tag{B.5}$$

and FFT can be used to carry out the inverse Fourier transform for optimal speed.

The gridding process to map non-Cartesian k-space data to Cartesian spatial domain pattern has been pointed out by Eq. B.5. First, the k-space data is convolved with some convolution kernel function C. Then, it is sampled on the Cartesian grid. A spatial domain pattern is then obtained using inverse FFT. Finally, the pattern is divided pixel-by-pixel by the inverse Fourier transform of the kernel function c.

Till now, the gridding formular is derived for the continuous case. In practical implementation, the spiral sampling function O_{Spr} is in discrete form and the integral

of convolution turns into summations. Thus, the integral interval changed from uniformly spaced $d\vec{k}$ to non-uniform interval $\Delta\vec{k}_j$. And a sampling density function W which is equivalent to $\Delta\vec{k}_j$ need to be added.

In addition, there are three more concerns in the implementation of gridding. First, a convolution kernel function need to be chosen. Functions such as Sinc function and Gaussian are potential choices. But it had been shown that the Kaiser-Bessel function can achieve minimum gridding error [23]. Second, since the convolution kernel can not be of finite support in the spatial domain, it will lead to aliasing artifact. The aliasing can be reduced by increasing the resolution of the Cartesian grid O_{Cart}. In the experiment of this work, we use an oversampling factor $\epsilon = 2$ and the spatial pattern is twice the size of FOX. Thus, truncation from the center of the pattern is need. Finally, this oversampling in k-space will uniformly scale up the intensity of the spatial domain pattern, an intensity correction step is necessary following the truncation of pattern. The scaling method is described in Appendix C.

APPENDIX C

INTENSITY CORRECTION FOR GRIDDING

The intensity correction is required in the last step of the gridding process to substitute the matrix-vector multiplication. The intensity scale is caused by the oversampling in k-space and it is uniform over the entire FOX. So suppose we can find a reference value at any spatial location, we can estimate the scaling factor.

Recall that the matrix-vector multiplication is given by,

$$\mathbf{m} = \mathbf{A}_{full}\mathbf{b} = \sum_{l} \mathbf{S}_l \mathbf{A} \mathbf{b}_l \tag{C.1}$$

where $\mathbf{A}$ is the Fourier encoding matrix with elements equal to $e^{i\vec{x}\vec{k}}$. So $\mathbf{A} = \mathbf{I}$ is the Identity matrix when $\vec{x} = 0$. Thus, the value of the pattern m at $\vec{x} = 0$ can be easily evaluated as

$$m(0) = \sum_{l} S_l(0) \sum_{j} b_l(t_j) \tag{C.2}$$

Then, the Cartesian pattern obtained from gridding operator G_1 is given by

$$m'(0) = G_1\{b_l[t], S_l[0], \vec{k}[t]\} \tag{C.3}$$

So the intensity correction scalor is found as $\dfrac{m(0)}{m'(0)}$. The intensity correction is not needed for the Hermitian transposed matrix-vector multiplication $\mathrm{A}_{full}^{H}\mathrm{m}$ using operator G_2 since zero padding will not change the amplitude of the k-space data.